The rat bladder umbrella cell keratin network: Organization, dependence on the plectin cytolinker, and responses to bladder filling

Wily G. Ruiz[a], Dennis R. Clayton[a], Tanmay Parakala-Jain[a], Marianela G. Dalghi[a], Jonathan Franks[b], and Gerard Apodaca[a,b,*]

[a]Department of Medicine Renal-Electrolyte Division and George M. O'Brien Pittsburgh Center for Kidney Research, University of Pittsburgh School of Medicine, Pittsburgh, PA; [b]Department of Cell Biology, University of Pittsburgh School of Medicine, Pittsburgh 15213

ABSTRACT **The keratin cytoskeleton and associated desmosomes contribute to the mechanical stability of epithelial tissues, but their organization in native bladder umbrella cells and their responses to bladder filling are poorly understood. Using whole rat bladders in conjunction with confocal microscopy, super-resolution image processing, three-dimensional image reconstruction, and platinum replica electron microscopy, we identified a cortical cytoskeleton network in umbrella cells that was organized as a dense tile-like mesh comprised of tesserae bordered by cortical actin filaments, filled with keratin filaments, and cross-linked by plectin. Below these tesserae, keratin formed a subapical meshwork and at the cell periphery a band of keratin was linked via plectin to the junction-associated actin ring. Disruption of plectin led to focal keratin network dissolution, loss of the junction-associated keratin, and defects in cell-cell adhesion. During bladder filling, a junction-localized necklace of desmosomes expanded, and a subjacent girded layer formed linking the keratin network to desmosomes, including those at the umbrella cell-intermediate cell interface. Our studies reveal a novel tile- and mesh-like organization of the umbrella cell keratin network that is dependent on plectin, that reorganizes in response to bladder filling, and that likely serves to maintain umbrella cell continuity in the face of mechanical distension.**

SIGNIFICANCE STATEMENT

- The organization of the keratin cytoskeleton in native tissues and its responses to mechanical distension are poorly understood.
- Working with rat bladder umbrella cells in vivo, the authors identified a cortical tile-like keratin network, a subjacent mesh-like keratin network, and a junction-associated band of keratin, that depended on the plectin cytolinker for their organization. During bladder filling, the keratin network and a junction-localized desmosomal necklace expanded, and a subjacent girded layer was formed that linked the keratin network to basal desmosomes.
- These studies reveal how the umbrella cell keratin network is organized and how it adapts to mechanical distension during bladder filling.

Monitoring Editor
Diana Toivola
Åbo Akademi University

Received: Jun 17, 2024
Revised: Sep 11, 2024
Accepted: Sep 24, 2024

INTRODUCTION

Umbrella cells, which form the superficial layer of the stratified urothelium, must adapt to large changes in wall tension as urine is stored and then voided while maintaining an impermeable barrier (Dalghi *et al.*, 2020). To understand how this is accomplished, one must identify the cellular structures and adaptations that make such a feat possible. Mechanisms described to date include changes in cell shape: umbrella cells become flat and squamous as the bladder fills but assume a somewhat cuboidal shape after voiding (Hicks, 1975; Truschel *et al.*, 2002). In addition, umbrella cells dramatically expand their apical surface area during filling (>100%), a consequence of exocytosis of membrane-rich discoidal/fusiform-shaped vesicles (DFVs) (Lewis and de Moura, 1982; Truschel *et al.*, 2002; Yu *et al.*, 2009), followed by the rapid and complete recovery of excess apical membrane by endocytosis in response to voiding (Yu *et al.*, 2009; Khandelwal *et al.*, 2010). Furthermore, components of the apical junctional complex (AJC), including the belt-like tight and adherens junctions and the AJC-associated actin belt undergo expansion during filling and contraction after voiding (Carattino *et al.*, 2013; Eaton *et al.*, 2019). The other major component of the AJC are desmosomes and associated keratin cytoskeleton; however, it is unknown how the bladder cycle impacts these structures. This is despite evidence that the keratin cytoskeleton imparts epithelial cells with mechanical strength and stability (Holthofer *et al.*, 2007; Hatzfeld *et al.*, 2017; van Bodegraven and Etienne-Manneville, 2021; Hegazy *et al.*, 2022; Schwarz and Leube, 2023) and that mutations in these components can lead to loss of cell cohesion and tissue integrity (McMillan and Shimizu, 2001; Holthofer *et al.*, 2007; Szeverenyi *et al.*, 2008; Pan *et al.*, 2013; Jacob *et al.*, 2018; Hegazy *et al.*, 2022).

In epithelial cells, keratins are organized in part by desmosomes, which are comprised of heteromeric assemblages of the transmembrane cadherin-family proteins desmocollin (DSC1-3) and desmoglein (DSG1-4), along with cytoplasmic components that include the following: the armadillo-family plakophilins (PKP1-3), the catenin plakoglobin (JUP), and desmoplakin (DSP), which links the desmosome complex to the keratin cytoskeleton. DSG2 and DSP are load sensing, indicating that desmosomes are likely sites of mechanotransduction (Baddam *et al.*, 2018; Price *et al.*, 2018; Bharathan *et al.*, 2024). While keratins often exhibit a loose mesh-like appearance, the desmosome-associated keratins are organized into functional "rim and spoke" components (Coch and Leube, 2016; Quinlan *et al.*, 2017; Tateishi *et al.*, 2017; Windoffer *et al.*, 2022). The spokes are comprised of radial keratin filaments, which run perpendicular to the plasma membrane, linking peripheral desmosome-attached keratins to the outer nuclear envelope, likely via the linker of nucleocytoskeleton and cytoskeleton complex (Stenvall *et al.*, 2022; Windoffer *et al.*, 2022). Thus, the spokes serve to support the cell in response to mechanical loads and convey instances of mechanical deformation to the nucleus. The "rim" component is comprised of a thin circumferential ring of keratin filaments that runs parallel to the plasma membrane, interconnects the desmosomes, and is hypothesized to assist in positioning and tensioning the desmosomes, particularly in response to mechanical deformations (Quinlan *et al.*, 2017; Prechova *et al.*, 2022). If other patterns of keratin organization exist remains an open question, but the keratin cytoskeleton of umbrella cells is reportedly akin to a woven mesh, with openings housing unfused DFVs, and with a "frame" of keratins at the cell periphery (Veranic and Jezernik, 2002). How keratin filaments are organized within the umbrella cell network, the relationship of the keratin network to AJC-associated desmosomes, and the nature of the keratin frame are unknown.

The functions and organizing principles of the rim and spoke keratins are not yet fully understood, but formation of rim-associated keratins depends on the presence of desmosomes and DSP, which bind and promote the elongation of keratins into rim (and spoke) components (Moch *et al.*, 2020). Moreover, a recent study implicates plectin (PLEC) in rim formation (Prechova *et al.*, 2022). PLEC is a large (>500 kD) ubiquitously expressed cytolinker that binds actin, keratin, and microtubules, recruiting them to a variety of organelles including mitochondria, the nucleus, and hemidesmosomes (Rezniczek *et al.*, 2016; Wiche, 2021). In cultured MDCK cells, knockout (KO) of *Plec* expression, or the use of a selective PLEC inhibitor called plecstatin-1 (Meier *et al.*, 2017), reveals roles for PLEC in mediating keratin–actin interactions at the AJC, formation of the keratin rim, organization of the spokes, planar arrangement of desmosomes, and overall monolayer cohesion (Prechova *et al.*, 2022). PLEC may also contribute to cell-cell adhesion, as conditional hepatocyte/cholangiocyte KO mice and conditional intestinal epithelial KO mice exhibit junctional defects (Jirouskova *et al.*, 2018; Krausova *et al.*, 2021). If PLEC plays a similar role in organizing the apical keratin network of native epithelia such as the urothelium remains to be described, although several epithelial tissues are known to express this protein (Wiche *et al.*, 1983).

Our studies reveal the organization of the keratin cytoskeleton, including desmosomes, in bladder umbrella cells, the role of PLEC in their organization, and the impact that bladder filling and voiding have on the keratin network. We discuss how the keratin network likely contributes to umbrella cell stability and cohesion during the bladder filling/voiding cycle.

RESULTS

AJC-associated desmosomes, comprised of DSG2 and DSC2, form a necklace-like structure that expands/contracts with bladder filling and voiding

When examined by thin-section transmission electron microscopy (TEM), the AJC of the rat bladder umbrella cells was comprised of readily identifiable tight junctions, adherens junctions, and desmosomes (Figure 1A). Positioned below the adherens junction, umbrella cell desmosomes had a characteristic ~25 nm gap (filled with electron-dense material) that formed between adjacent cells and were bordered on their cytoplasmic surfaces by a dense plaque-like material (Farquhar and Palade, 1963). A mass of cytoskeletal filaments (labeled "Csk" in Figure 1A) was observed adjacent to the desmosomes, but also along the entire aspect of the AJC. Single-cell transcriptomic data obtained from closely related mouse

This article was published online ahead of print in MBoC in Press (http://www.molbiolcell.org/cgi/doi/10.1091/mbc.E24-06-0262) on October 2, 2024.

Author Contributions: G.A., W.G.R., D.R.C., and M.G.D. conceived and designed the experiments; G.A., W.G.R., D.R.C., T.P.-J., and M.G.D. analyzed the data; G.A. and M.G.D. drafted the article; G.A., W.G.R., D.R.C., and M.G.D. prepared the digital images; W.G.R., D.R.C., T.P.-J., M.G.D., and J.F. performed the experiments.

Conflicts of interest: The authors declare no financial conflict of interest.

*Address correspondence to: Gerard Apodaca (gla6@pitt.edu).

Abbreviations used: AJC, apical junctional complex; DFVs, discoidal/fusiform-shaped vesicles; KO, knockout; PREM, platinum replica electron microscopy; SEM, scanning electron microscopy; SRIP, super-resolution image processing; 3D, three-dimensional.

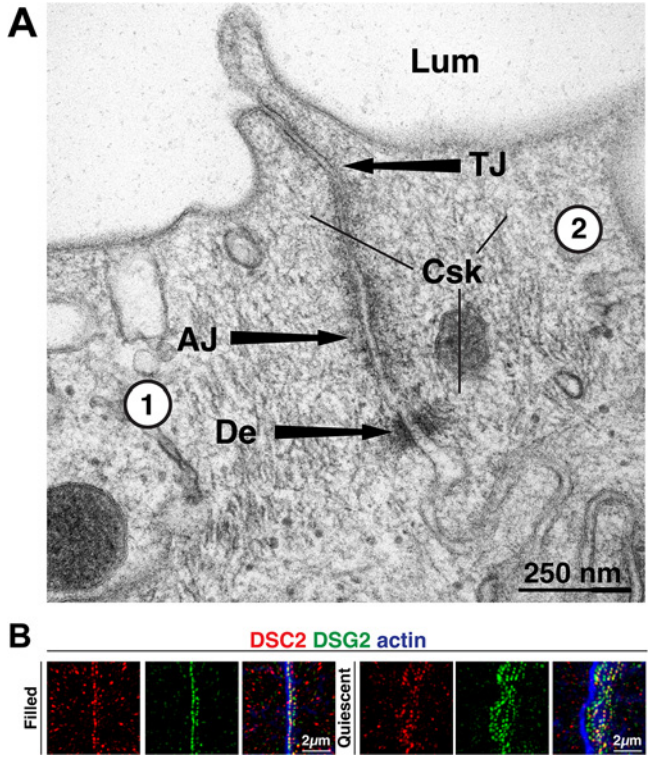

FIGURE 1: Bladder umbrella cell desmosomes. (A) Thin-section TEM of rat bladder umbrella cells. An AJC-associated desmosome (De) is localized below the adherens junction (AJ) and tight junction (TJ) of two adjacent cells (labeled 1 and 2). Legend: Csk, cytoskeletal filaments; Lum, lumen. (B) Expression of DSC2 and DSG2 at the AJC of two adjacent umbrella cells taken from filled or quiescent bladders. Images are 3D reconstructions of confocal Z stacks. AJC-associated desmosomes are found to the left of the image, and lateral ones are found to the right. Phalloidin was used to label the AJC-associated actin ring, which is positioned above the AJC-associated desmosomes (to the left), and to label the cortical actin cytoskeleton along the lateral surfaces (extending to the right). As the lateral signal is weak, it is barely visible it in these images.

umbrella cells indicate that *Dsg2* and *Dsc2* are likely the sole or major desmosomal cadherins expressed by these cells (Yu *et al.*, 2019), and we confirmed that DSG2 and DSC2 were coexpressed in spot-like structures at the interface of adjacent rat umbrella cells, both at the AJC and along the lateral membranes (Figure 1B).

To better understand the organization of the desmosomes in the umbrella cell AJC, we performed confocal microscopy, coupled with super-resolution image processing (SRIP; nominal resolution of 120 nm), and three-dimensional (3D) surface rendering of whole-mounted tissue taken from bladders filled to half their capacity (0.5 ml in rats of this age/weight; see supplemental Video 1). Unless otherwise noted, these are referred to as filled bladders in the subsequent discussion. This analysis revealed that the desmosomes could be discriminated from the apical-most tight junction labeled with tight junction protein 1 (TJP1, aka ZO1) and from the belt of actin that lay between TJP1 and the adherens junction (Figure 2, A and B). The latter is associated with the upper one-third of cadherin1 (CDH1; aka E-cadherin) staining, whereas the lower two-third of CDH1 staining was associated with the lateral membranes of the umbrella cell and overlapped with DSG2. The desmosomes had a beaded appearance and were situated at the interface between adjacent urothelial cells. We identified three populations of desmosomes in umbrella cells. The first of these were AJC-associated (magenta-colored in Figure 2). These were found just below the adherens junction and are equivalent to the AJC-associated desmosomes identified by TEM above (Figure 1A). These desmosomes formed a necklace-like structure that surrounded the apex of the cell. However, at the tricellular region of the AJC, which characteristically exhibits a dip in junction height (see arrowheads in Figure 2A) (Higashi and Miller, 2017), DSG2 was absent from its base (see also yellow arrow, bottom inset, Figure 3A). In contrast, TJP1, actin, and CDH1 formed continuous belts. The second population of desmosomes, those along the lateral surfaces of the umbrella cell, were sparser and did not form a necklace-like structure (cyan-colored in Figure 2, B and C). The third population, found at the base of the umbrella cell, formed sites of cell-cell contact between umbrella cells and the underlying intermediate cells (blue-colored in Figure 2, B and C).

Like the umbrella cell tight junction and adherens junction (Eaton *et al.*, 2019), we observed that the AJC-associated necklace of desmosomes expanded during filling and shrank after voiding (Figure 3A). Absent of the waviness of the cell borders in voided bladders, the continuity and organization of AJC-associated desmosomes were not obviously affected by these events (Figure 3, A and B). In either case, we observed a continuous necklace of desmosomes surrounding the cell periphery (excluding regions at the base of tricellular junctions). While the average surface area of individual desmosomes was significantly larger in voided bladders, differences in their volume did not reach significance (Figure 3C). Concordant with the greater cell perimeter of filled versus voided umbrella cells (Figure 3C), the average number of AJC-associated desmosomes per cell was significantly greater in umbrella cells taken from filled bladders (~600) versus voided ones (~200) (Figure 3C). However, when the number of AJC-associated desmosomes per μm of perimeter length was calculated, there was no significant difference between filled and voided bladders (Figure 3C). This may indicate a cellular mechanism that holds the ratio of desmosomes/cell perimeter length relatively constant even in the face of large changes in cell perimeter as the bladder fills and empties. In sum, like the tight and adherens junction, the umbrella cell's necklace of desmosomes also accommodates the bladder's filling and voiding cycle.

The umbrella cell keratin cytoskeleton is organized in distinct apical and basal layers. To further explore the organization of the umbrella cell keratin network, we localized KRT20 in cross-sections of urothelium derived from filled bladders or quiescent ones (the latter were emptied, but not allowed to fill). Umbrella cells from filled bladders exhibited a squamous morphology, while those of quiescent bladders had a roughly cuboidal shape (Figure 4A). The apical surface of the latter often exhibited a wavy/ruffled appearance (Figure 4A). In either case, KRT20 amassed at the apical pole of umbrella cells forming a relatively thick mesh-like structure, while less KRT20 was found at the basal pole of the cells (Figure 4A). The underlying intermediate (and basal cells) were KRT20 negative.

The complexity of the KRT20 network became apparent when whole-mounted urothelium, obtained from filled bladders, was viewed from above using confocal-SRIP microscopy and 3D surface reconstruction (see supplemental Video 2). At the periphery of each umbrella cell, we observed a thin continuous band of KRT20 that collected on either side of the AJC-associated actin ring (see yellow arrowheads in middle right panel of Figure 4B). This band

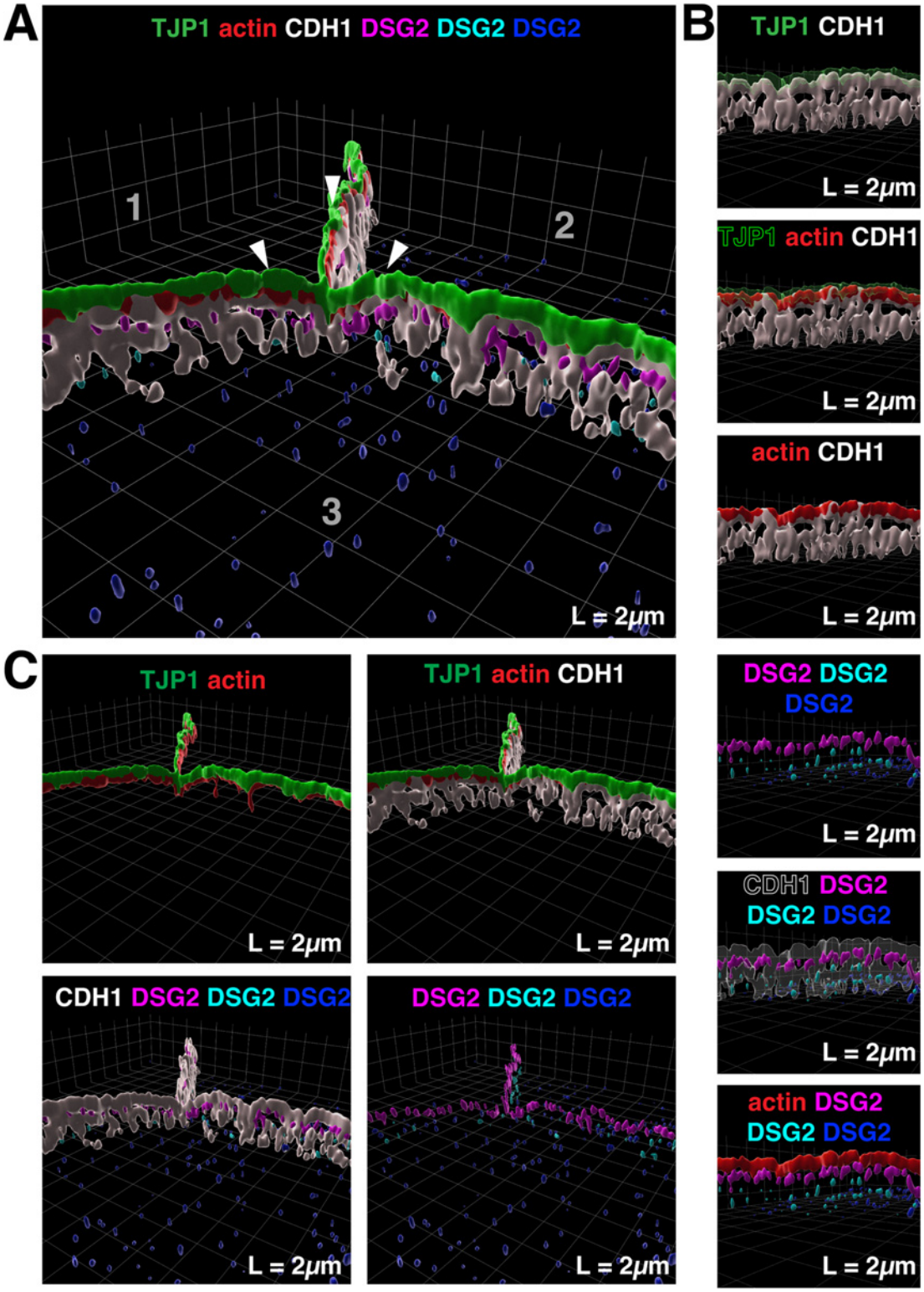

FIGURE 2: 3D reconstruction of the umbrella cell AJC. (A) 3D surface reconstruction of a confocal-SRIP Z-stack taken at the tricellular region of three adjacent umbrella cells (labeled 1–3) obtained from a filled bladder. Arrowheads indicate the site where the tricellular junction dips. (B) The larger image was rotated along its lateral axis and digitally sliced to allow a head-on view of the AJC in the bicellular region between two cells. In some images, one of the markers is made transparent to allow viewing the underlying/overlapping signal. The transparent signal is indicated by outlined text. (C) Additional views of tight junction, adherens junction, AJC-associated actin belt, and desmosomes. DSG2-labeled desmosomes were classified as being AJC associated (magenta), lateral surface associated (cyan) or located at the interface of umbrella cells and subjacent intermediate cells (dark blue). Video: See companion Video 1 for 3D rendering of AJC.

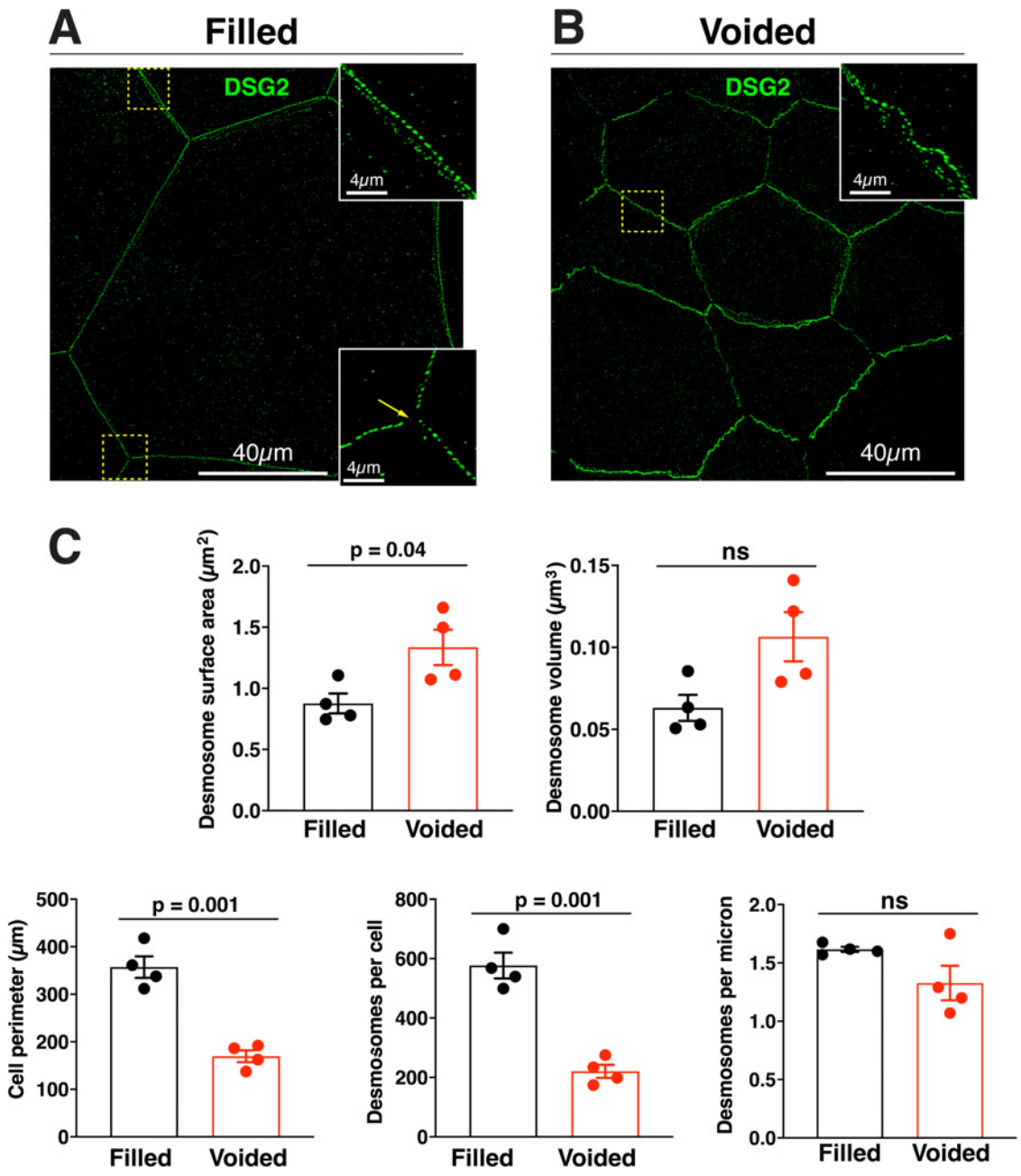

FIGURE 3: Effects of bladder filling and voiding on the AJC-associated desmosome necklace. (A and B) Examples of DSG2-labeled umbrella cells taken from filled (A) or voided (B) bladders imaged using confocal-SRIP microscopy and rendered in 3D. The boxed regions are magnified in the insets. Note that the AJC-associated desmosomes are those facing the top-right corner. The yellow arrowhead in the bottom inset of panel A indicates the site of the tricellular junction. (C) Quantification of the indicated parameters for filled and voided bladder umbrella cell desmosomes. Desmosome surface area and volume refer to average values for individual AJC-associated desmosomes obtained from 3D datasets. Cell perimeter refers to the average values for the perimeter of individual umbrella cells. Desmosomes per cell are averages of the total number of AJC-associated desmosomes associated with an individual umbrella cell. Desmosomes per micron is the obtained by dividing the average number of desmosomes per cell by the respective mean value for the cell perimeter. Data are mean ± SEM ($n = 4$ animals). The p values for significant differences are given, and nonsignificant differences are indicated by "ns."

of KRT20 likely corresponds to the "frame" described previously (Veranic and Jezernik, 2002). Analysis of 3D surfaces revealed that the peripheral band of KRT20 extended up to the level of the AJC-associated actin ring (rightmost panels, Figure 4B), although the KRT20 band was sometimes shorter. Away from the AJC, we observed that the keratin network was polarized along the apical-basal axis, forming two somewhat overlapping layers, which were best visualized in individual X-Y sections taken from confocal Z-series. An apical "mesh-like layer" composed of interlaced keratin strands was observed at the apical pole of the cell. In umbrella cells

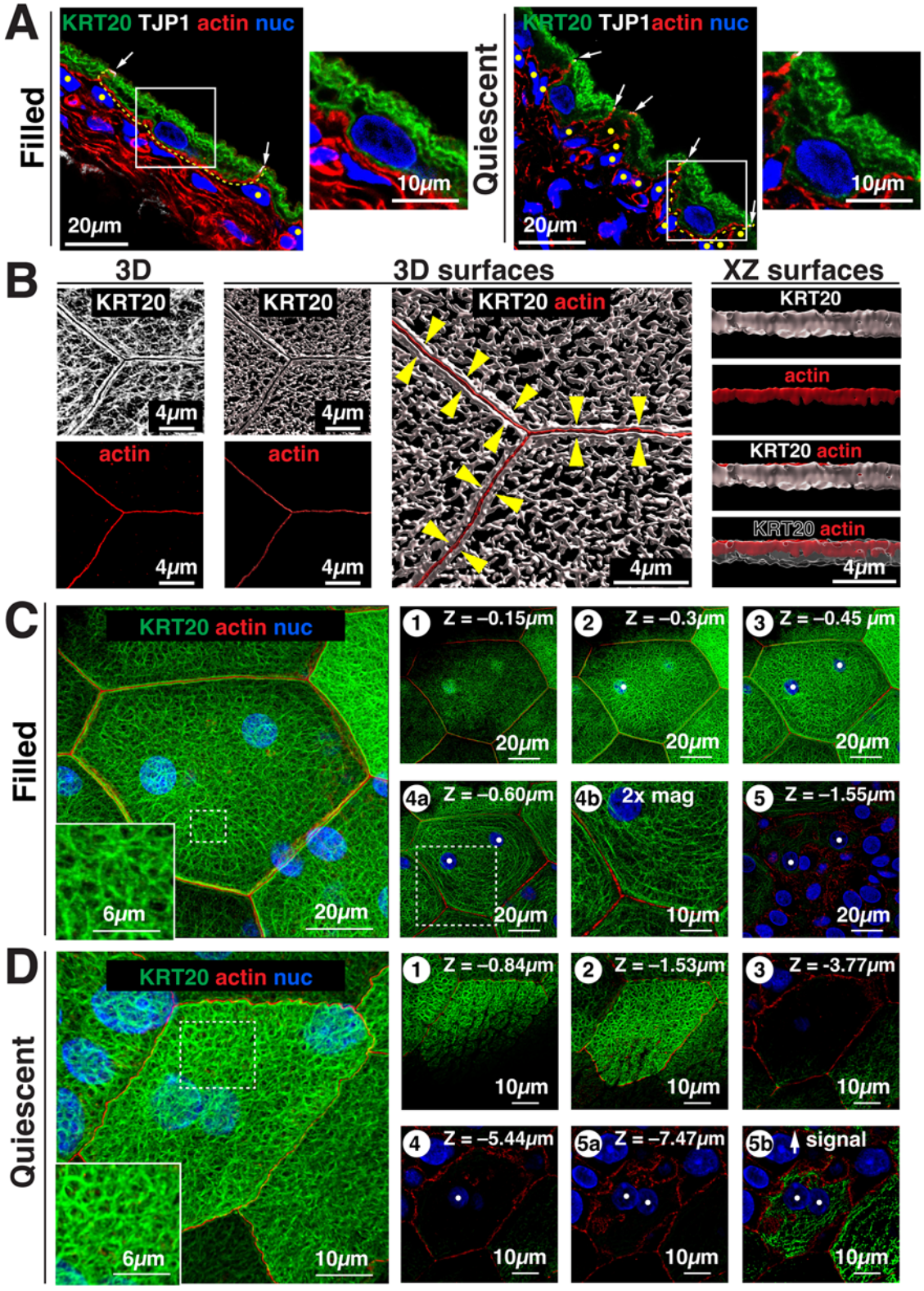

FIGURE 4: Organization of the keratin network in umbrella cells obtained from filled and quiescent bladders. (A) Filled and quiescent bladders were cryosectioned and the urothelium immunolabeled as indicated. The outline of the basolateral surface of an individual umbrella cell is indicated by a yellow dashed line. White arrows point to the location of the AJC, and the boxed regions are magnified in the smaller panels to the right of the larger images. In the filled bladder, the smaller image shows the central portion of an umbrella cell, while the smaller image in the quiescent bladder shows an entire umbrella cell. Underlying intermediate cells are indicated by yellow circles. (B) Reconstruction of the umbrella cell KRT20-labeled network in 3D or as 3D surfaces (derived from confocal-SRIP images obtained from

taken from filled bladders, two circular-shaped bumps of keratin were often observed in the upper portion of the mesh layer, which were positioned directly above the paired nuclei of these cells (see subpanel 1 in Figure 4C).

Below the mesh layer of these filled bladders, and extending deeper into the cytoplasm, was a basal "girded layer" comprised of keratin filaments that in X-Y sections were organized in a belt-like pattern of nested ovals that followed the contours of the cell perimeter (see subpanels 3 and 4a in Figure 4C). The ovals were cross-linked by struts comprised of perpendicularly arranged keratin filaments (see 2X magnified subpanel 4b in Figure 4C; see also supplemental Video 3). In these filled bladder preparations, the upper aspects of each of the umbrella cell's two nuclei were embedded within these nested ovals, apparently connecting the nuclear ectocytoskeleton to the keratin network. However, there was relatively less keratin signal associated with the basal pole of these nuclei (see subpanel 5 in Figure 4C and supplemental Video 3). Given that keratin filaments are comprised of heteromers of acidic and basic keratins (Jacob *et al.*, 2018), it was not surprising that KRT8 (a basic keratin) and KRT20 (an acidic keratin) shared an overlapping distribution in umbrella cells (Supplemental Figure S1); however, KRT8 was also expressed by the underlying intermediate and basal cell layers. We also assessed the organization of KRT20 in umbrella cells in which the bladder was filled to capacity (1.0 ml). The umbrella cell layer remained patent, the cells were very flat, they exhibited maximal diameters, and their keratin network appeared similar to what is described above (Supplemental Figure S2). However, the girded layer was more pronounced in these cells, possibly indicating more recruitment of keratin to this layer to support the increased wall tension.

We also explored the keratin network in the umbrella cells of quiescent bladders. In these preparations, the umbrella cells exhibited apical folding (apparent as discontinuities of the keratin network when individual optical sections are examined; for example, see subpanels 1 and 2 in Figure 4D), and like filled bladders, the apical keratin network had a mesh-like appearance (Figure 4D; supplemental Video 4). Strikingly, there was an absence of a visible girded layer in quiescent umbrella cells and relatively little KRT20 signal was found associated with the nuclei of these cells or at their basolateral pole (Figure 4D; supplemental Video 4). However, KRT20 could be detected in these regions if the signal intensity was boosted (see subpanel 5b in Figure 4D).

In sum, our initial confocal analysis revealed that the keratin network in umbrella cells is comprised of an apical mesh-like layer and a subjacent girded layer. The latter is not observed in quiescent bladders but develops in response to bladder filling and is presumably a mechanism to maintain tissue cohesion in the face of increased wall tension.

The umbrella cell KRT20 network interacts with AJC-associated and basolateral desmosomes

We next sought to understand the relationship of the umbrella cell keratin network with desmosomes. Foci of DSP were localized to either side of DSG2-labeled desmosomes, giving the impression of parallel, registered, and dashed lines of DSP when adjacent cells were viewed from above (Figure 5A). 3D surface reconstructions revealed that DSP and DSG2 were roughly within the same Z-plane and the tripartite structure was oriented parallel to the cell surface (see Figure 5, A and B). These reconstructions further revealed that between cell-cell junctions the peripheral band of KRT20 formed a fjord-like structure with DSP-DSG2 at its base (see supplemental Video 5). XZ slicing further confirmed that the peripheral band of KRT20 (along with most of the apical mesh layer) extended above the DSP/DSG2-labeled desmosomes (Figure 5B); although, the lower quarter of the KRT20 band overlapped with DSP (Figure 5B), and which may serve as potential sites of KRT20 anchorage.

To better understand the sites of KRT20–desmosome interaction, we scrutinized X-Y optical sections taken from the tricellular region of filled bladders. In Z planes with the brightest DSP signal, we observed that the basal aspects of the peripheral KRT20 band came near the AJC-associated DSP signal (leftmost upper panel in Figure 5C). In addition, KRT20 struts emanated from either side of the junction that linked the AJC-associated keratin to the remaining mesh-like network. The straight appearance of these struts is consistent with keratin filaments under tension (Fudge *et al.*, 2008). In the girded layer, the KRT20 filaments associated with the nested ovals appeared to be organized by contact with desmosomes at the umbrella cell/intermediate cell junction (middle and leftmost upper panels of Figure 5C). In quiescent bladders, we observed that the KRT20 band near the AJC-associated desmosomes was offset a small amount from the DSP signal by what appeared to be short struts or cross-bridges that connected to filaments that ran parallel the membrane (see inset in bottom rightmost panel of Figure 5C). At the base of the quiescent umbrella cells, a small fraction of basal desmosomes appeared to associate with KRT20 filaments (lower middle panel of Figure 5C).

In sum, the keratin network of umbrella cells taken from filled bladders likely interacted with desmosomes at two sites: (i) those within the AJC/lateral membrane and (ii) those at the base of the umbrella cells. At the AJC, the interaction was of a rim-and-strut type that connected the keratin network to the mesh layer, whereas at the base of the cells the girded layer of keratin appeared to be organized by interactions with desmosomes at the umbrella cell:intermediate cell interface. In quiescent umbrella cells, keratin interactions with the AJC-associated desmosomes were observed, while interactions with basal desmosomes were less pronounced.

filled bladders). Yellow arrowheads in the rightmost center image indicate the band of keratin at the cell periphery. Panels to the right: the adjacent overview image to the left was rotated 90°along its lateral axis and digitally sliced allowing for a head-on view of just the region of the keratin band near the AJC. In the lower panel, the signal for KRT20 is rendered transparent to reveal the location of the rearward actin ring. The KRT20 text label is outlined in this case. (C and D) Organization of the KRT20-labeled network in an umbrella cell taken from a filled bladder (C) or a quiescent bladder (D) and imaged using confocal-SRIP microscopy. Subpanels to the right are individual X-Y-sections taken at the indicated depth (apical-most section was set to Z = 0). (C) Leftmost image: the boxed region is magnified in the inset. In the right-most panels, the position of nuclei is indicated by white dots. The boxed region in subpanel 4a is magnified 2-fold in subpanel 4b. (D) Leftmost image: the boxed region in the image is magnified in the inset. The KRT20 signal in subpanel 5a is increased in subpanel 5b. Videos: Companion videos show the apical-most aspect of the keratin network of umbrella cells taken from filled bladder (supplemental Video 2) or the girded layer (supplemental Video 3). A video is also presented for an umbrella cell taken from a quiescent bladder (supplemental Video 4).

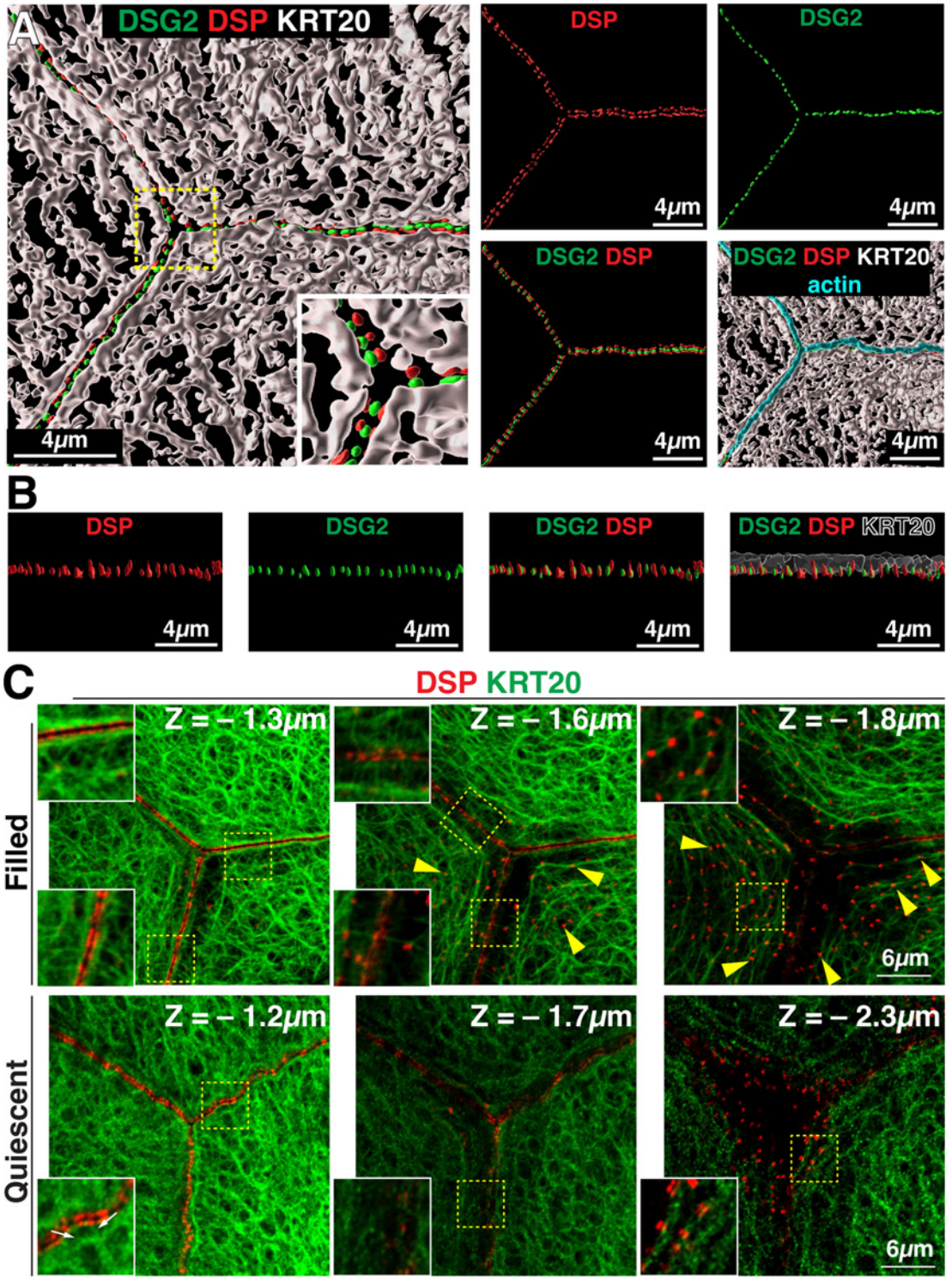

FIGURE 5: Localization of DSG2, DSP, and KRT20 in umbrella cells of filled and quiescent bladders. (A) 3D surface reconstruction of confocal-SRIP Z-stack showing the distribution of DSG2, DSP, KRT20, and the AJC-associated actin ring of filled bladder umbrella cells. (B) The upper left image was rotated 90° along its lateral axis and digitally sliced allowing for a head-on view of just the region of the AJC-associated desmosomes and KRT20 network. Rightmost panel: the KRT20 signal is rendered transparent to allow viewing the overlap of this signal and that of DSG2/DSP. (C) A tricellular region of the umbrella cell layer, taken from filled or quiescent bladders, was imaged using confocal-SRIP microscopy. X-Y sections at the indicated Z level are shown (apical-most section is Z = 0). Boxed regions are magnified in the insets. Yellow arrowheads indicate examples of close association between the girded layer and desmosomes at the umbrella cell/intermediate cell junction. Small white arrows in lower left panel indicate short keratin struts in quiescent samples connecting the desmosomes and the adjacent KRT20 mesh. Video: A companion video shows the 3D relationship between the apical keratin network and the DSP/DSG2-labeled desmosomes (supplemental Video 5).

Electron microscopy of umbrella cells reveals an apical cortical cytoskeleton organized as a dense tile-like mesh comprised of keratins, actin, and cytolinkers

Electron microscopy of detergent-extracted and cytoskeleton-stabilized tissue was used to further explore the ultrastructure of the keratin network and other cytoskeletal elements at the umbrella cell apical cortex (i.e., the interface between the apical-most elements of the cytoskeleton and the apical membrane). Using scanning electron microscopy (SEM), individual umbrella cells were identified by the presence of the AJC, which encircled the cell and appeared as a raised ridge (~400 nm in width) at the cell periphery from which filaments extended on either side (Figure 6, A–C). At higher magnifications, a closely packed mesh of filamentous cytoskeletal elements became apparent (Figure 6, B–D). The filaments had a diameter of ~20 nm, although the nominal deposition of ~2.5–4.0 nm of gold-palladium would place these in the range of 12–15 nm, indicating many were intermediate filaments. However, it is not possible to reliably distinguish keratins from actin (or microtubules) in these images. Most filaments appeared straight, extending for 50–400 nm, but some were curved. Thinner filaments with a nominal diameter of ~11 nm (actual diameter 3–6 nm) were also observed, as were thicker cables ~30–55 nm (actual diameter 22–50 nm). The latter were sometimes hydra like, branching into smaller diameter fibers.

The microarchitecture of the filament network varied to some degree by cellular location. At the region of the tricellular junction, a dense network of crisscrossed or woven filaments was observed to form an inverse Reuleaux triangle (three-sided polygon; Figure 6C). Reflecting the very close apposition of membranes and cytoskeletal elements at the tight junction, it was not possible to make out individual cell borders in this or other regions of the AJC. At the periphery of the tricellular junction, the ~20 nm filaments were oriented parallel to the junction, but others appeared to extend away from the junction in a perpendicular manner. The latter ones likely attached the AJC to adjacent filaments in the network (Figure 6C). The bicellular regions of the AJC shared many of the features of the tricellular AJC including the lack of identifiable cell borders and a dense network of filaments some of which ran parallel to the junction while others extended away from the junction in a perpendicular manner (Figure 6, D and E). Again, the latter attached the bicellular junction to the main network. We also observed lacunae (i.e., small spaces or gaps) that opened toward the apical surface and had walls comprised of crisscrossing fibers that encapsulated the opening (Figure 6, D and E). These are likely to be equivalent to the "stomata" described by Veranic and Jezernik that house clusters of DFVs prior to their fusion (Veranic and Jezernik, 2002). A small number of filaments was observed to extend across the lacunal opening (yellow arrows in Figure 6E). Lacunae were present across the apical region of the mesh but were often found in close proximity to the AJC (Figure 6, D and E), indicating that the AJC may be a site of active exocytosis.

Away from the AJC, the cortical cytoskeletal mesh appeared to be organized somewhat akin to a mosaic comprised of tesserae (tile-like structures) encased by bordering elements and filled with ~20 nm filaments (for examples, see false-colored regions in Figure 6F). The size of the resulting tesserae varied: small ones had areas of $\leq$1.0 μm^2, but larger ones had areas approaching several microns (5–8 μm^2). The bordering elements had lengths on the order of ~0.5–2.0 µm (but sometimes extending 5 or more microns) and diameters of ~75–200 nm (examples of bordering elements are demarcated by white arrowheads in Figure 6F). The constituents of bordering elements were sometimes difficult to assess as these elements were most likely to retain proteins during the extraction process; however, in regions devoid of attached proteins a filamentous substructure was apparent. The ~20 nm diameter filaments that filled each tessera appeared to span the bordering elements, forming an elaborate crisscross pattern, or in some cases generating a central hub with emanating spokes (see white arrows in Figure 6F).

To gain more insights into filament identity and organization, we turned to platinum replica electron microscopy (PREM) (Svitkina, 2016); which we adapted for use on native urothelial tissue (see *Materials and Methods*). In addition to aiding our recognition of keratin filaments, it also allowed us to identify short, small-diameter cytolinkers (e.g., PLEC), and to reveal the actin cytoskeleton by decorating it with myosin heavy chain S1 fragments (Ishikawa *et al.*, 1969). We first examined the region near the AJC, which in PREM appeared flatter than by SEM, but could be identified by its continuous belt-like architecture, its width of 200–400 nm, and its granular appearance when viewed from above (it is color-coded blue in Figure 7A). Short, unbranched actin filaments (typically <1.0 µm in length; color-coded red in Figure 7A) with random polarity were observed to insert into the bicellular AJC and in some cases appeared to ride above it. Keratin filaments were identified by their nominal diameter of ~16 nm (actual diameter of ~12 nm accounting for the ~2 nm platinum coating) and are color-coded green in Figure 7A. At higher magnifications, they had the appearance of a dense pipe cleaner. Keratin filaments were observed to insert into the AJC at acute angles or they paralleled the long axis of the AJC. Away from the AJC, the keratins appeared crisscrossed. The other notable structures at the AJC were small-diameter fibers (~6 nm nominal diameter, ~2 nm actual diameter), with lengths of ~50–200 nm, which we tentatively identified as cytolinkers (orange-colored structures in Figure 7A). They primarily cross-linked the intermediate filaments to one another, but some extended from the AJC to adjacent filaments. These appear similar if not identical to PLEC cytolinkers previously described, which are reported to have diameters of ~2–3 nm and measured lengths of 50–200 nm (Foisner and Wiche, 1987; Foisner *et al.*, 1995; Svitkina *et al.*, 1996). At the region of the tricellular junction, we again noted short, randomly oriented actin filaments accumulating near the junction, as well as the presence of keratin filaments and short cytolinkers (Figure 7B).

Given the AJC-associated actin ring and the peripheral band of KRT20 identified by confocal microscopy, it was surprising that there was no obvious concentration of actin or keratins near the AJC as visualized by PREM. As PREM (and SEM) only allows for a surface view of the sample, we examined cross-sections of PREM-processed samples (minus the final platinum coating) using standard thin-section TEM. This revealed large numbers of 11-nm keratin filaments extending up to 500 nm on either side of the detergent-resistant, electron-dense core of the tight junction (Figure 7C). The latter was identified using antibodies to TJP1. The nature of this electron dense core was not explored further. Although, these cross-sectioned samples were also S1 treated, we did not observe decorated actin filaments associated with the AJC either because they were not resolvable from the dense accumulation of intermediate filaments, or because they were oriented in a manner that did not allow their identification. However, occasional decorated actin filaments (identified by their sympodial branching appearance in thin-section EM) could be found in proximity to the AJC (see black arrowheads in Figure 7C). To further explore the organization of actin at the AJC, we immunolocalized S1-labeled

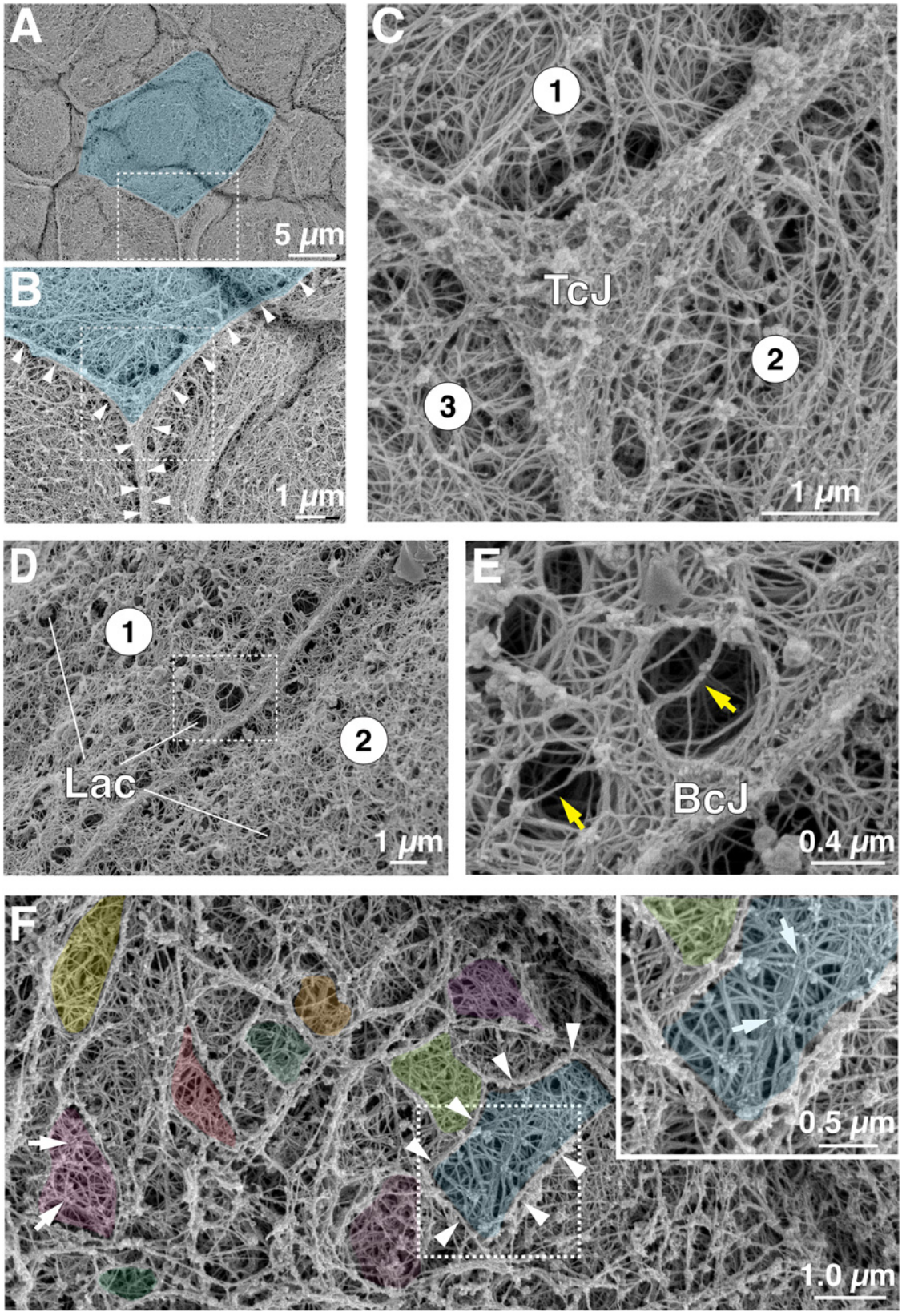

FIGURE 6: SEM analysis of the cytoskeletal network at the AJC and apical cortex of umbrella cells. (A) Overview of umbrella cell cortical cytoskeleton revealed by detergent extraction, cytoskeleton stabilization, and SEM. An individual umbrella cell is false-colored blue. The boxed region is magnified in panel B. (B and C) The region of the tricellular junction (TcJ) is magnified. White arrowheads in panel B indicate the position of cell-cell borders. The boxed region in B is magnified in panel C. The circled numbers indicate the three cells that join to form this region of the umbrella

actin using confocal-SRIP microscopy. This confirmed actin localization to the AJC (Supplemental Figure S3A), and further revealed perpendicular struts of actin that connected the AJC to an adjacent cortical actin network that extended across the apical surface of the umbrella cell (struts are indicated by arrowheads in the middle panel of Supplemental Figure S3A). No signal was detected in samples not incubated with S1 fragments but otherwise treated identically (rightmost panel, Supplemental Figure S3A). While the actin struts and the apical cortical network of actin were not detected by phalloidin labeling (e.g., see Figure 4B), it is worth noting that phalloidin binding depends on the conformation of actin, can be obscured by actin-binding proteins, and detecting/resolving individual actin filaments by confocal microscopy can be difficult (Ao and Lehrer, 1995; McGough *et al.*, 1997; Rondanino *et al.*, 2007).

The nature of the cortical cytoskeletal network was further revealed by PREM, which showed that the bordering elements defining each tessera were composed of filamentous actin, arranged as single filaments or as parallel bundles of two or more actin filaments (Figure 8A and arrowheads in Figure 8B). PREM further revealed that the central portions of each tessera were filled with keratins in a crisscrossed or woven pattern extending for short runs and then apparently terminating near actin filaments or passing below these elements to connect with the underlying keratin mesh (Figure 8C). The likelihood of the latter is supported by two observations. First, TEM cross-sections through the extracted network revealed that the cortical actin filaments were intimately associated with underlying keratins (Figure 8D) and a small mass of electron dense material of unknown composition was observed at these points of interaction (yellow asterisks in Figure 8D). Second, by immunolocalizing S1-labeled actin and KRT20 using confocal-SRIP microscopy, KRT20 was observed in the central portions of S1-labeled actin tesserae, but the keratin filaments appeared to extend beyond the actin bordering elements forming a larger-diameter keratin meshwork than that of the actin cytoskeleton (see insets in Supplemental Figure. S3B). PREM also revealed that individual actin filaments were interspersed among the keratin filaments, and cytolinkers were observed that connected the keratin filaments to one another and adjacent bordering elements (Figure 8C). Finally, we observed that the walls of lacunae were formed of keratin filaments (sometimes curved), along with short actin filaments, cytolinkers, and unidentified bordering elements (Figure 8E). Individual actin filaments and keratins along with cytolinkers were observed to intersect the opening of lacunae. This observation is consistent with a previous report that small numbers of actin and intermediate filaments are closely allied with DFVs in freeze deep-etch preparations (Terada *et al.*, 2009).

In summary, our ultrastructural analysis reveals that the apical cortical cytoskeleton of umbrella cells is organized in a tile-like pattern, with tesserae bordered on their edges by actin filaments and filled with crisscrossed/woven keratin filaments (apparently connected to an underlying keratin network) and cross-linked by cytolinkers. Tesserae are interrupted by lacunae, which likely house unfused DFVs. Finally, the peripheral band of keratin identified in confocal studies was revealed to be a mass of keratins that accumulated on either side of the tight junction, but also extended deep to the desmosomes.

Impairment of PLEC function causes keratin and actin reorganization, and loss of cell cohesion

Given the importance of cytolinkers such as PLEC in organizing keratin networks (Svitkina *et al.*, 1996; Wiche, 2021), coupled with the presence of PLEC-like structures in our PREM studies, we sought to determine whether PLEC was involved in organizing the native umbrella cell keratin network. Using confocal-SRIP, coupled with 3D surface reconstruction, we identified two general pools of PLEC in umbrella cells. The first one was positioned above the DSG2-labeled desmosomes where it concentrated along either side of the AJC-associated actin ring (colored green in Figure 9A; supplemental Video 6). Furthermore, we observed that at sites of cell-cell adhesion, the AJC-associated band of KRT20 was positioned to either side of the AJC-associated PLEC, forming a pentalaminar KRT20-PLEC-actin-PLEC-KRT20 structure (Figure 9B). The second pool of PLEC was distributed across the apical pole of the cell, where it appeared to be closely associated with the KRT20 mesh (non-AJC PLEC is colored dark blue in Figure 9, A and B). This is consistent with our PREM studies in which we observed PLEC-like cytolinkers that were associated with the mesh layer of keratins. Unfortunately, we were unable to immunolocalize PLEC in PREM samples, but as noted above the cytolinkers we observed by PREM bore the hallmarks of PLEC (Svitkina *et al.*, 1996).

PLEC binds keratins by way of a C-terminal intermediate filament-binding domain but can also bind to actin via an N-terminal actin binding domain (see Figure 10B) (Nikolic *et al.*, 1996; Andra *et al.*, 1998). Thus, we hypothesized that PLEC may serve to organize the AJC-associated band of keratin by linking it to the actin ring. As an initial test of this possibility, we asked whether the actin disrupting agents cytochalasin D (CytoD) or the actin-depolymerizing agent latrunculin A (LatA) impacted the organization of the keratin and PLEC networks in stretched bladder samples. CytoD treatment resulted in the accumulation of large aggregates of actin throughout the umbrella cell cytoplasm (Supplemental Figure S4); however, the AJC-associated actin ring remained intact. PLEC was recruited to a subset of the CytoD-induced actin aggregates (see white arrows in Supplemental Figure S4), and PLEC staining at the AJC appeared somewhat broader and less tight than that observed in control, DMSO-treated cells (compare PLEC vs. DMSO in Supplemental Figure S4). Despite these effects, CytoD treatment had no obvious impact on the peripheral band of keratin or the overall apical keratin mesh. LatA (used at concentrations of 1–50 μM) did not alter the localization of PLEC or KRT20. Thus, it was unclear whether LatA was inhibitory, as it had no obvious effect on the umbrella cell actin cytoskeleton. PLEC also binds to and organizes the microtubule cytoskeleton (Svitkina *et al.*, 1996), which was previously implicated in tight junction homeostasis (Glotfelty *et al.*, 2014). In umbrella cells, microtubules were found embedded in the keratin mesh (Supplemental Figure S5A), and non-AJC PLEC appeared to be in close apposition to microtubules (Supplemental Figure S5B), but few microtubules were associated with the AJC (Supplemental Figure S5C). Treatment with the microtubule depolymerizing-agent nocodazole had no visible effect on PLEC or the keratin cytoskeleton (Supplemental Figure S4).

cell layer. (D and E) Organization of cytoskeleton near the bicellular junction (BcJ) of two cells labeled 1 and 2. Examples of lacunae (Lac) are indicated. The boxed region in D is magnified in panel E. Yellow arrows in panel E indicate sparse cytoskeletal elements that traverse the lacunal opening. (F) Region of cortical cytoskeleton away from the AJC. Examples of tesserae are false-colored in the larger image. White arrows indicate regions of mesh where 20 nm filaments are organized as a central hub with emanating spokes. Boxed region is magnified in inset.

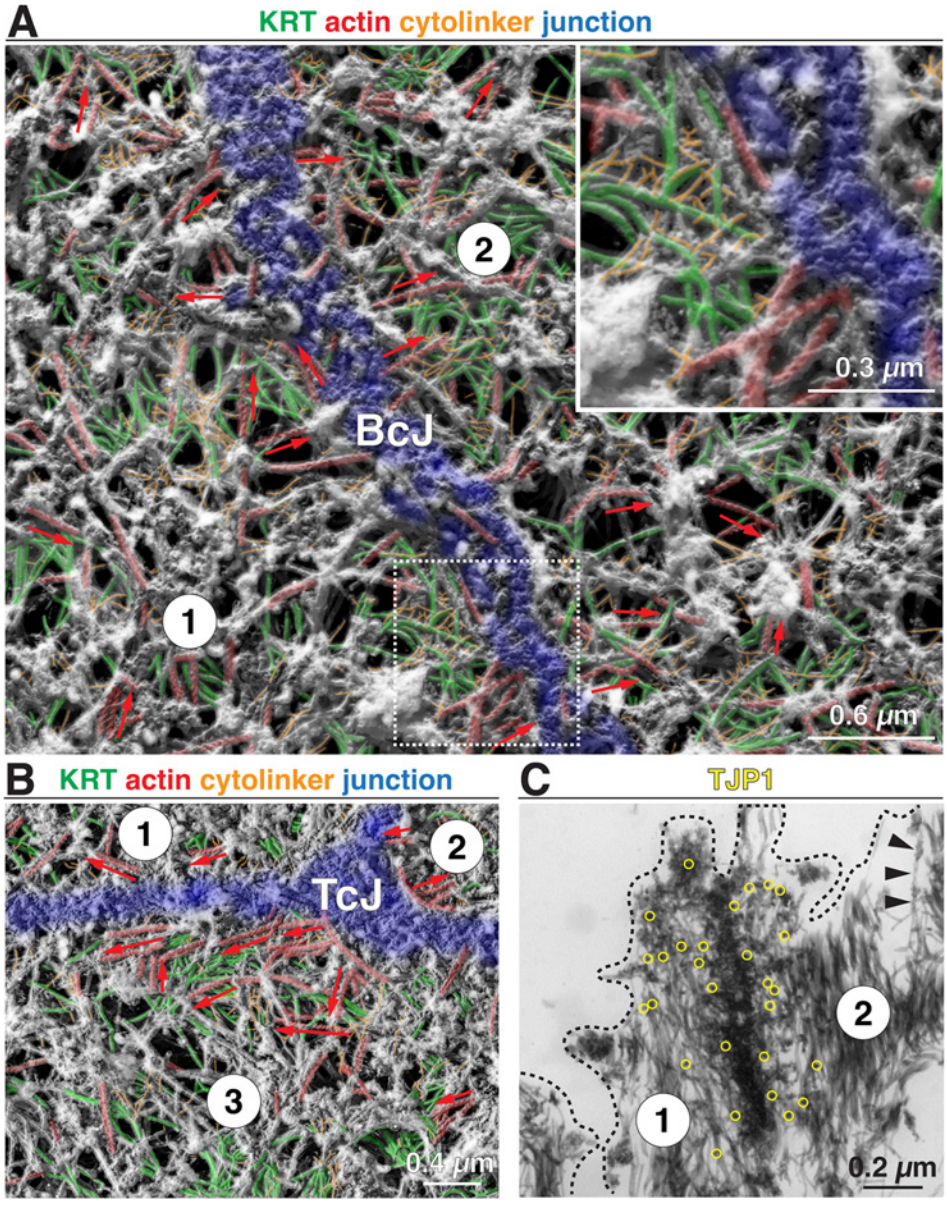

FIGURE 7: PREM analysis of umbrella cell cortical cytoskeleton near the AJC. (A) Cytoskeleton near the bicellular junction (BcJ). The junction itself is false-colored blue, actin is colored red, keratin filaments are green, and cytolinkers are colored orange. Unidentifiable filaments lack false coloring. Red arrows indicate the orientation of actin filaments with the tip of the arrow indicating the pointed end of the S1-decorated filament. The boxed region is magnified in the inset. (B) Cytoskeleton network near the tricellular junction (TcJ). (C) Thin section TEM of cytoskeletal network near the AJC. Localization of TJP1 (incubated with 12 nm gold-conjugated secondary antibodies) is indicated by yellow circles. Black arrowheads indicate an S1-decorated actin filament. The approximate position of the plasma membrane is indicated by the black dashed line.

We also used a dominant-negative approach to assess PLEC–actin interactions. PLEC has multiple N-terminal splice variants, which regulate the recruitment of the cytoskeleton to distinct cellular compartments (e.g., nucleus, focal adhesions, hemidesmosomes) (Fuchs *et al.*, 1999; Castanon *et al.*, 2013; Wiche, 2021). PLEC1, PLEC1a, PLEC1c, and PLEC1f variants are reportedly expressed by epithelial cells (Fuchs *et al.*, 1999), and in MDCK cells PLEC1a and PLEC1f were recently shown to be integral to recruitment of rim-associated keratins and the organization of desmosomes (Prechova *et al.*, 2022). We used RT-PCR to confirm expression of *Plec1*, *Plec1a*, *Plec1c*, and *Plec1f* variants in mouse urothelium and rat umbrella cells (Figure 10A; Supplemental Figure S6). Using this information, we generated two constructs. The first was PLEC1a-8-EGFP, a construct that encoded exon1a of *Plec* along with its complete actin-binding domain (ABD; encoded by exons 2–8) fused to EGFP (Figure 10B). This construct was expected to act in a dominant-negative manner by competing for binding of endogenous PLEC to the actin cytoskeleton. The second construct was PLEC1a-6-8-EGFP, a nominal control construct, which lacked the first calponin homology domain and is reportedly inefficient at binding actin (Figure 10B) (Fuchs *et al.*, 1999; Fontao *et al.*, 2001).

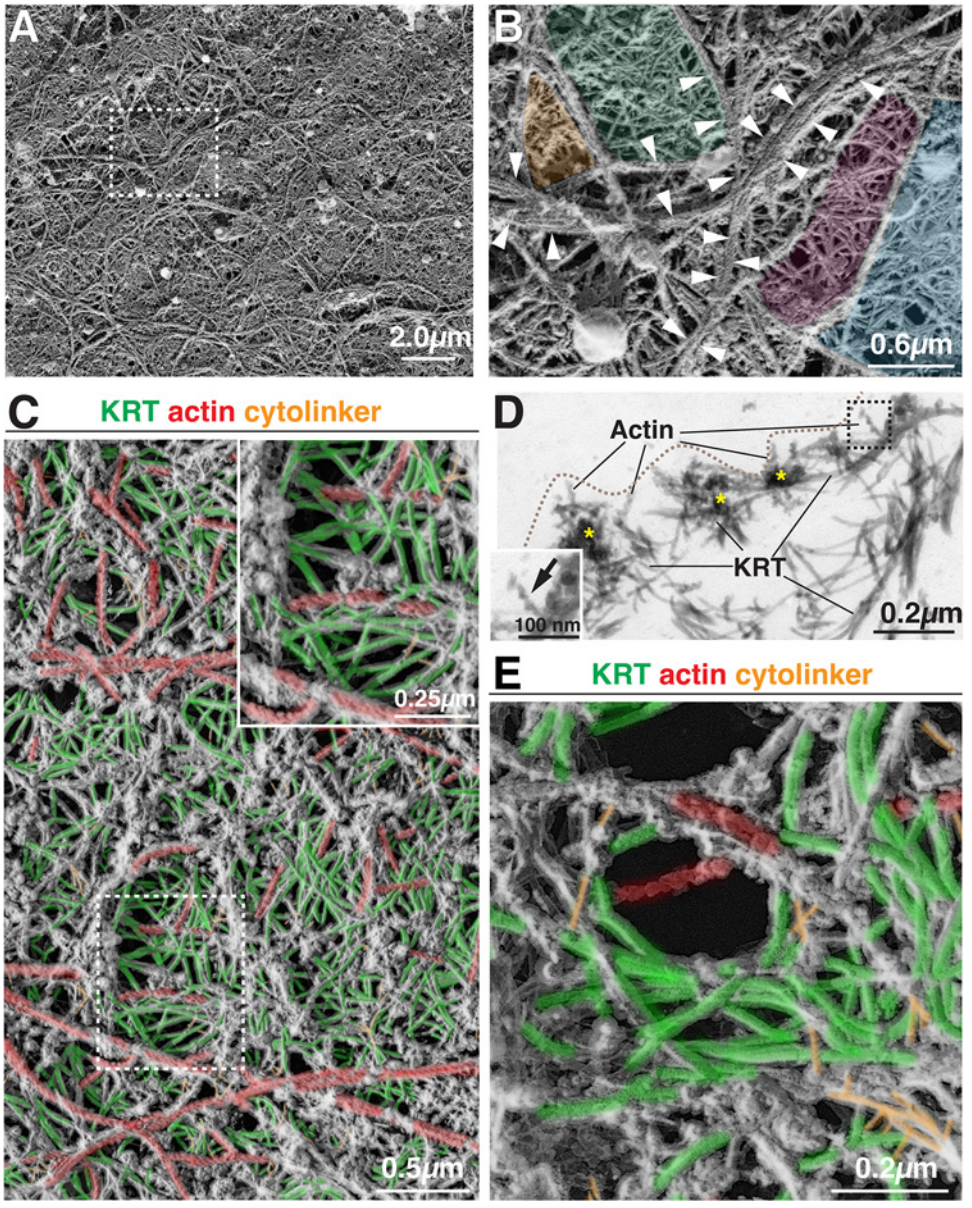

FIGURE 8: Organization of umbrella cell apical cortical cytoskeleton network revealed by PREM. (A and B) Tile-like organization of cortical cytoskeletal network. The actin filaments bordering tesserae were often arranged in parallel bundles of two or more actin filaments (indicated by short white arrows in panel B). Example tesserae are false colored in panel B. (C) Overview of the cortical cytoskeleton at the apical pole of the umbrella cell. (D) TEM cross section through tesserae revealing the associated actin filaments (facing the apical membrane, which is marked by the dashed line) and subjacent keratin (KRT) filaments. Electron dense material connecting these two filament systems are indicated by yellow asterisks. Boxed region shows an example of an S1-decorated actin filament. (E) Organization of cytoskeleton surrounding lacunae. In C and E, actin is colored red, keratin filaments are green, and cytolinkers are colored orange. Unidentifiable filaments lack false coloring.

Because of ease of transduction, we used mouse bladders in the following studies. Upon transducing the umbrella cell layer with the PLEC1a-8-EGFP–encoding virus, we observed the expected recruitment of the expressed construct to the region of the AJC (Figure 10C), but we also observed a filamentous pool of the construct that was just apparent above the background signal (see EGFP signal in the bottom panel, Figure 10C). The actin cytoskeleton in these cells was perturbed including the appearance of actin filaments in the cytoplasm near the base of the cells. Intriguingly, the AJC-associated keratin band was absent in cells expressing this construct (Figure 10C), although the apical keratin mesh had a generally normal appearance. In addition, we noted the appearance of keratins at the points of cell-cell adhesion that were straight and in alignment with filaments on the adjoining cell ($Z = -8.6$ μm in Figure 10C), consistent with the cells being under a mechanical load. A small fraction of cells (~20%) was observed to express large amounts of this construct and these cells formed a juxtanuclear cytoplasmic aggregate that was actin and KRT20 positive (cells marked with an asterisk in rightmost panels of Figure 10C). We also observed a loss of PLEC staining near the AJC in cells expressing

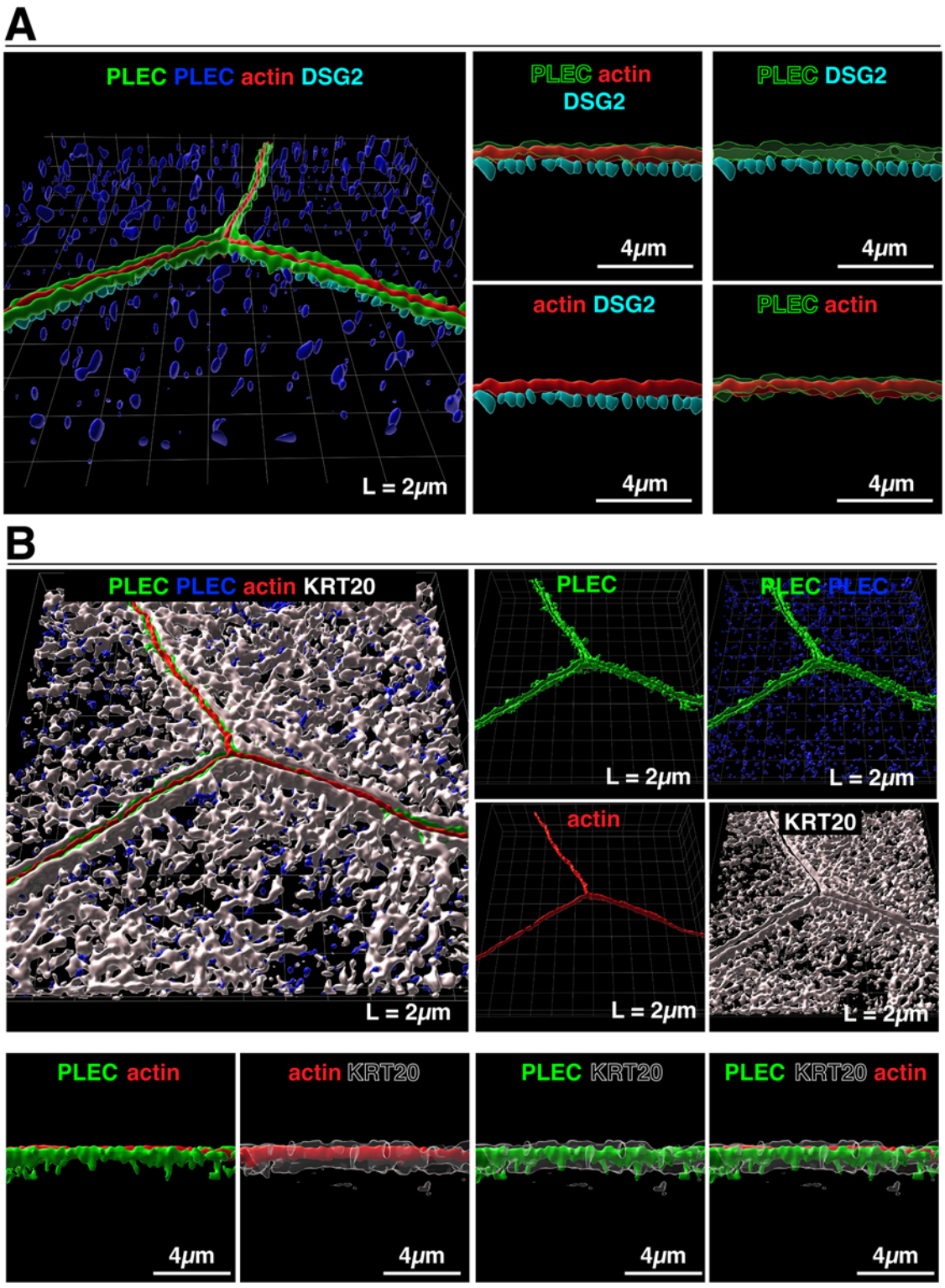

FIGURE 9: Distribution of PLEC in umbrella cells from filled bladders. (A) Leftmost image: 3D surface reconstruction of PLEC, AJC-associated actin, and DSG2-labeled desmosomes using data from a confocal-SRIP Z-stack. PLEC signal associated with the AJC is colored green and PLEC associated with the KRT20-labeled mesh is colored dark blue. Rightmost images: The larger image to the left was rotated along its lateral axis and digitally sliced allowing a head-on view of a bicellular region of the AJC. In these images, PLEC is rendered transparent to allow viewing the underlying signal. (B) Upper left image: relationship of PLEC to the KRT20 mesh. Upper-right images: signal for the indicated markers are displayed. Lower images: the larger image in the upper left was rotated along its lateral axis and digitally sliced allowing a head-on view of a bicellular region of the AJC. In these images, KRT20 is rendered transparent to allow viewing the underlying signal. Video: A companion video shows the 3D organization of the plectin cytolinker with respect to the AJC (supplemental Video 6).

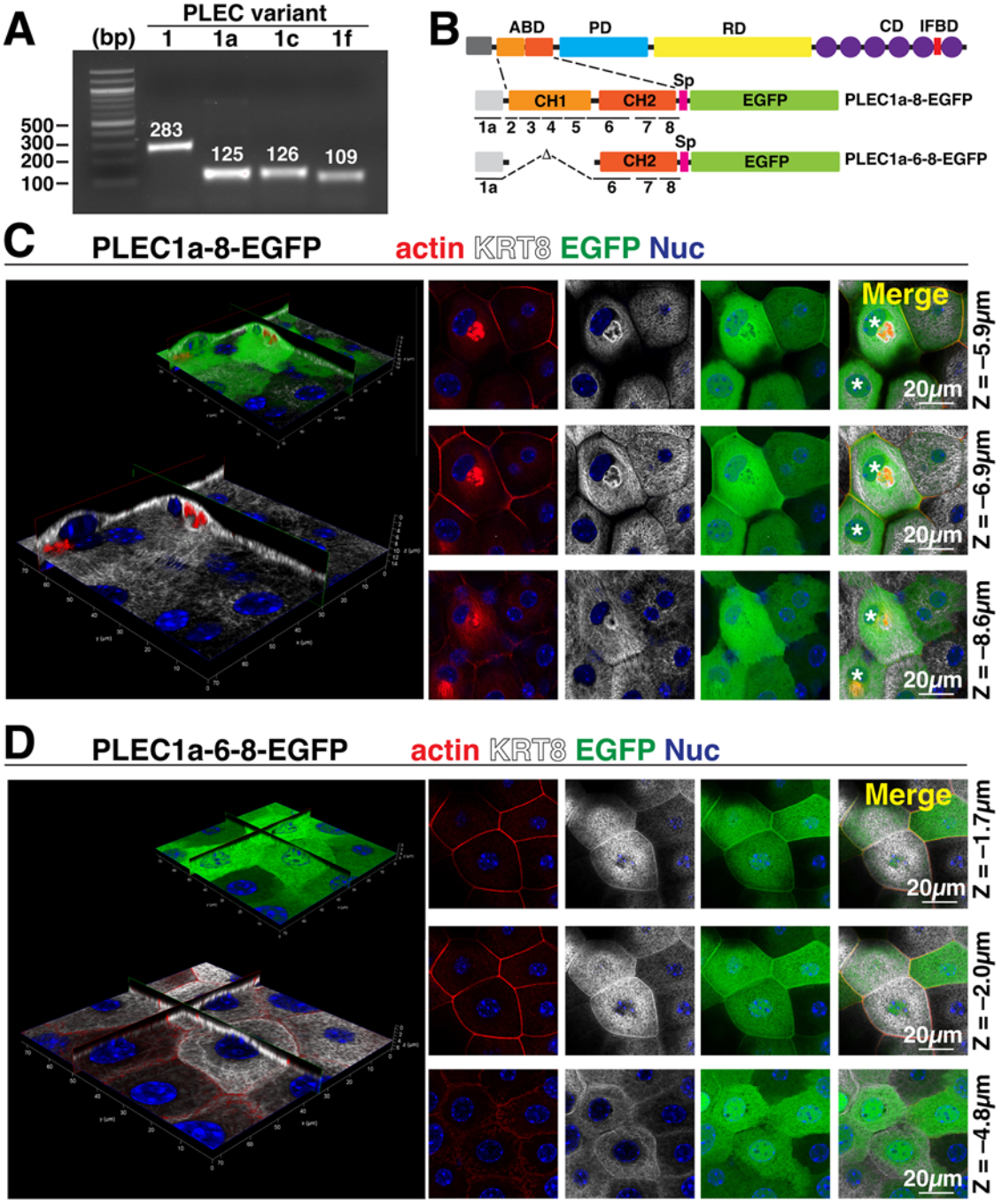

FIGURE 10: Impact of expressing a dominant negative PLEC construct on the umbrella cell keratin cytoskeleton. (A) Use of PCR to assess expression of the indicated PLEC mRNA splice variant in mouse urothelium. The expected size of the amplicon (in bp) is indicated in white text. (B) Domain structures of PLEC and the PLEC constructs used in these experiments (not drawn to scale). Numbers below the constructs indicate the approximate location of the exon boundaries of the *Plec1A* variant. Legend: ABD, actin-binding domain; CD, C-terminal plectin-repeat domain; CH1/2, calponin homology domain 1/2; EGFP, enhanced green fluorescent protein; IFBD, intermediate filament binding domain; PD, plakin domain; RD, coiled-coil rod domain; Sp, spacer (flexible linker). (C and D) Mouse bladders were transduced with adenoviruses encoding a dominant-negative PLEC1a-8-EGFP construct (C) or the control PLEC1a-6-8 construct (D). The impact of expression of the indicated construct on the actin cytoskeleton and KRT8 cytoskeleton was assessed using confocal microscopy. Larger, leftmost images: 3D reconstruction of a confocal Z-stack dissected using orthogonal slicers. Expression of the EGFP-tagged construct is shown in the smaller image in the upper right of the panel. Smaller images: Individual X-Y sections taken at the indicated distance along the *Z*-axis (topmost image set as Z = 0). The white asterisks in the merged panel for C are examples of two cells that expressed high levels of the construct and exhibit a juxtanuclear aggregate of actin.

this construct, but not in adjacent untransduced cells (Supplemental Figure S7). The control PLEC1a-6-8-EGFP construct had an overall cytoplasmic appearance, although some of it was recruited to the region of the AJC (Figure 10D). If this reflects binding via sequences encoded by PLEC exon 1a, or weak adhesion to the actin ring was not assessed. However, in cells expressing this construct we did not observe the development of actin-rich cytoplasmic aggregates or actin fibers, and the apical keratin mesh and band of keratin near the AJC were not affected in these cells (Figure 10D). Furthermore, we noted minimal loss of PLEC staining at the AJC of cells expressing this control construct (Supplemental Figure S7).

To further explore a functional role for PLEC in the organization of the umbrella cell keratin cytoskeleton we turned to plecstatin-1, a newly described antitumor drug that selectively targets PLEC and which mimics the effects of *Plec* KO in MDCK cells (Meier *et al.*, 2017; Prechova *et al.*, 2022). When the urothelium was treated with 25 μM plecstatin-1, we noted cells with focal abnormalities in the organization of their keratin and actin cytoskeletons. These changes included the formation of actin- and PLEC-rich foci that formed in the central portions of the cells or at sites along the bicellular and tricellular junctions (Figure 11, A and B). These foci exhibited a corresponding decrease in KRT20 signal, leaving discontinuities in the keratin network including loss of the AJC-associated keratin band in affected cells (see white asterisks in merged panel of Figure 11A). These lesions were also accompanied by discontinuities in the tight junction (marked by CLDN8; Supplemental Figure S8A) and loss of cell-cell cohesion (yellow arrows in merged image, Figure 11A). In some case, we observed regions where umbrella cells were missing, revealing the underlying intermediate cells (see dashed region in the upper row, leftmost panel of Supplemental Figure S8A). When plecstatin-1–treated cells were examined by PREM, the foci were revealed to be mesa-like structures that were often elevated and had a flat top with few associated cytoskeletal elements (data not shown and Supplemental Figure S8B). Surrounding the mesa were accumulations of woven actin, as well some keratins and cytolinkers (Supplemental Figure S8C). Scattered lacunae were observed in these regions. Taken together, these studies reveal that PLEC function is integral to the organization of the umbrella cell keratin cytoskeleton, and that disruption of PLEC function leads to formation of mesa-like foci that are characterized by focal disassembly of the keratin mesh, loss of the AJC-proximal band of keratin, compensatory changes in the actin cytoskeleton, AJC dysfunction, and loss of umbrella cell cohesion.

DISCUSSION

The keratin cytoskeleton and associated desmosomes are key contributors to epithelial stability and cohesion (Hatzfeld *et al.*, 2017; Latorre *et al.*, 2018; Hegazy *et al.*, 2022). Yet, we have few insights into the organization of the umbrella cell keratin cytoskeleton, the adaptations that the umbrella cell keratin cytoskeleton makes in response to bladder filling, or the molecules that regulate this network. Our studies reveal the following: (i) that the umbrella cell keratin cytoskeleton includes cortical tile-like elements, a subjacent apical meshwork, and an AJC-associated component; (ii) that the plectin cytolinker is integral to the continuity of the umbrella cell keratin cytoskeleton and PLEC dysfunction leads to focal keratin loss and umbrella cell de-adhesion; (iii) and that bladder filling and the attendant increase in wall tension leads to a reorganization of the umbrella cell desmosome/keratin network including formation of a basally localized girded layer. Taken together, these observations support the likelihood that the umbrella cell keratin cytoskeleton contributes to umbrella cell mechanical stability and function during the bladder filling/voiding cycle.

The keratin networks of epithelial cells such as HaCaT keratinocytes, MDCK cells, native retinal pigment epithelial cells, and blastocysts are organized as loose "fishnet-like" meshes (Quinlan *et al.*, 2017; Windoffer *et al.*, 2022). Integral to these meshes, is a rim-and-spoke architecture in which thicker keratin filaments (i.e., spokes) connect desmosomes to the nucleus and fine keratin filaments (i.e., rims) interlock the desmosomes (Quinlan *et al.*, 2017). Other patterns of keratin organization exist. For example, in enterocytes, keratins are observed to accumulate at the apical pole of the cell where they are observed to cross-link the actin-rich rootlets of microvilli (Hirokawa *et al.*, 1982; Oriolo *et al.*, 2007), and during mouse airway development, keratins form a thin mesh that surrounds the basal bodies of ciliated airway cells (Tateishi *et al.*, 2017). In the case of umbrella cells, the apical cortical cytoskeleton is organized into tesserae filled with woven keratin filaments, cross-linked by cytolinkers (likely PLEC), and bordered by actin filaments. The cortical keratin filaments appear to extend deep to the cortex where they are incorporated into a subjacent apical mesh. This mesh is the most prominent feature of the umbrella cell keratin network when viewed from above. Interupting the tesserae and subjacent meshwork are lacunae, which are proposed to house DFVs prior to fusion (Veranic and Jezernik, 2002).

The other prominent component of the umbrella cell apical keratin network is a thin band of keratin, originally described as a "frame" (Veranic and Jezernik, 2002), that abuts the AJC and which we revealed by confocal-SRIP microscopy and thin-section EM to be an accumulation of keratin filaments on either side of the tight junction and AJC-associated actin ring. The function(s) of this keratin band is unknown, but it could serve as a reserve of keratin filaments that would allow the umbrella cell to expand during bladder filling (and then function as a site of storage after voiding), or it may be a site of keratin nucleation/assembly. The keratin band does not obviously function as a "rim" in the sense that it is positioned above the desmosomes and instead appears to be organized by the PLEC cytolinker, which is sandwiched between the AJC-associated actin ring and the keratin band. Thus, in addition to previous reports that PLEC regulates rim keratins, spokes, and associated desmosomes in MDCK cells (Prechova *et al.*, 2022), our data reveal that in native umbrella cells PLEC organizes the overall keratin network as well as the AJC-associated keratin band and actin cytoskeleton. Our data further support reports that PLEC is integral to AJC continuity and cell-cell adhesion (Jirouskova *et al.*, 2018; Krausova *et al.*, 2021), as plecstatin-1–treated umbrella cells exhibit focal dissolution of the AJC-associated actin cytoskeleton and a corresponding loss of tight junction continuity, eventually leading to a loss of cohesion.

Our studies, and those of others, also revealed several adaptations that the umbrella cell's keratin network makes during bladder filling, and which are likely to contribute to urothelial cell and tissue continuity. The first adaptation is related to the properties of keratin filaments and the reported thinning of the bordering elements of the keratin mesh observed in filled bladders (Veranic and Jezernik, 2002). In this regard, keratins are known to straighten when stretched, they exhibit elasticity (reaching strains up to 100% and are also compressible), and they resist breakage by becoming stiffer as strain increases (Ma *et al.*, 1999; Kreplak *et al.*, 2005; Fudge *et al.*, 2008). The mechanical behavior (elasticity and/or stiffness) of filaments such as keratins depends in part on the relationship between their contour length (L_c) and persistence length

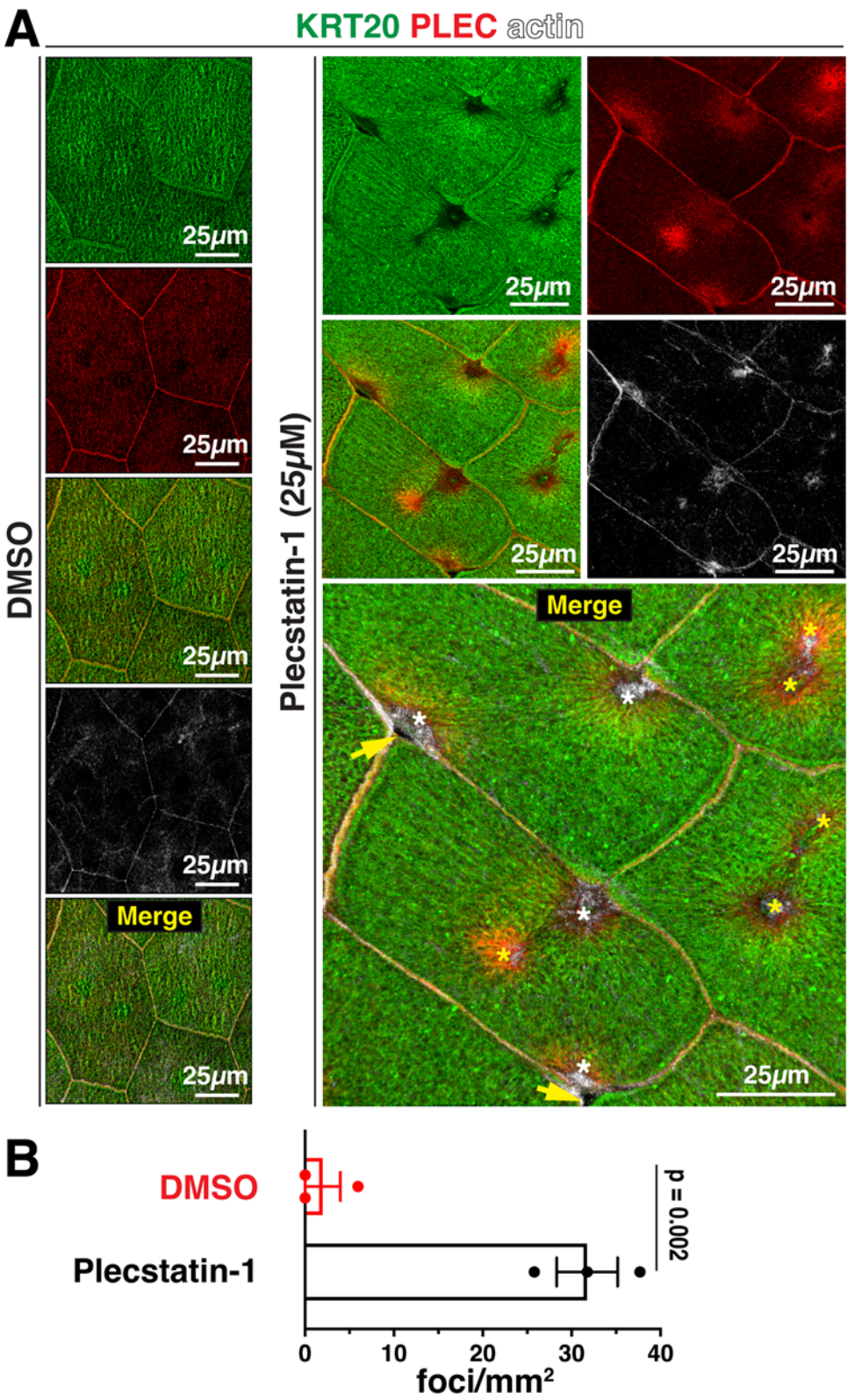

FIGURE 11: Effect of plecstatin-1 on the cytoskeletal network of umbrella cells. (A) Stretched bladder tissue was treated with 25 μM plecstatin-1 or DMSO solvent for 60 min at 37°C. A 3D reconstruction of a Z-volume obtained using confocal microscopy was generated. In the merged panel, yellow arrows indicate regions of lost cohesion, white asterisks are examples of mesa-like foci forming near the AJC, and yellow asterisks are mesa-like foci forming in the central regions of the cell. (B) Quantitation of the number of PLEC^{+} phalloidin^{+} foci/mm^{2} detected in stretched bladder tissue treated with 25 μM plecstatin-1 or DMSO solvent. Data are mean ± SEM ($n = 3$). Values were significantly different ($p = 0.002$).

(L_p; i.e., bending stiffness) (Picu, 2011; Yang *et al.*, 2022). Given the reported persistence length of keratins (~0.3 μm) (Mucke *et al.*, 2004), and the contour length of keratins within tesserae (~0.5 μm), these fibers can be classified as semiflexible (defined as $L_P \cong L_C$). However, the presence of cross-links (e.g., those mediated by PLEC) would alter the L_P/L_C relationship because L_C is measured between cross-linked segments and when $L_P >> L_C$ a less flexible and stiffer fiber is formed. Thus, by altering PLEC cross-links, one could regulate the stiffness of the umbrella cell keratin network. This would be particularly relevant at the apical cortex, which sits at the interface between the cytoskeleton and apical membrane and must accommodate the mechanical forces associated with bladder filling/voiding. The actin cytoskeleton is also likely to contribute to the mechanical properties of the umbrella cell. For example the actin filaments bordering tesserae may serve to stiffen the overall network as the L_p of actin is ~18 μm (Gittes *et al.*, 1993), and the length of the actin bordering elements is variable but on the order of 0.5–2 μm (thus $L_P >> L_C$). However, the association of cortical actin filaments with the umbrella cell apical membrane may result in softening as is described for spectrin networks in erythrocytes (Gov, 2007). Likewise, the short actin filaments (typically <1.0 μm) we observed interspersed throughout the tile-like network, in lacunae, and near the junctions may also serve to stiffen the network.

The second adaptation is expansion of the desmosome necklace to further accommodate the increase in surface area and change in cell shape, as well maintain tissue cohesion. Given our previous studies of the tight junction and adherens junctions (Eaton *et al.*, 2019), it is likely that expansion of the desmosomal necklace is driven in part by actin polymerization and exocytosis of junction components such as DSG2 and DSC2. However, it is possible that it may also involve the reversible recruitment of desmosomes from the basolateral surfaces of the umbrella cell. In contrast, shrinking of the cell perimeter in response to voiding would likely entail nonmuscle myosin II–mediated contraction and endocytosis of desmosomes, which has been studied in other settings (Burdett, 1993; Holm *et al.*, 1993; Demlehner *et al.*, 1995; Chen *et al.*, 2012). By extension, it is possible that new keratin mesh is synthesized or assembled during the bladder filling phase and returned to a baseline state soon after voiding.

The third adaptation is the ability of the keratin network to support the exocytosis of large numbers of subapical DFVs in response to filling, thereby allowing for surface expansion. There is evidence that intermediate filaments regulate organellar and vesicular traffic (Ameen *et al.*, 2001; Ivaska *et al.*, 2005; Perrot and Julien, 2009; Potokar *et al.*, 2010; Margiotta and Bucci, 2016). We previously reported that DFV maturation likely involves a Rab11a-Rab8a cascade whereby $Rab11a^+$ DFVs, which predominate in the keratin network, mature into a release-ready pool of $Rab8^+$ DFVs (and a separate subpool of $Rab27b^+$ DFVs) that accumulate below the apical membrane (Khandelwal *et al.*, 2013; Gallo *et al.*, 2018). Given previous reports of actin and keratin association with DFVs in lacunae (Veranic and Jezernik, 2002; Terada *et al.*, 2009), it is possible that these cytoskeletal elements promote DFV maturation. Moreover, the elastic nature of keratin filaments may allow rapid and facile penetration of the keratin mesh in the situation whereby DFVs undergo massive exocytosis (Yu *et al.*, 2009).

The fourth adaptation, and perhaps the most striking change we observed in response to filling, is the formation of a girded layer as umbrella cells transition from a "cuboidal" morphology to a squamous one. Comprised of nested ovals of keratin filaments, the girded layer is a site of keratin attachment to the desmosomes at the AJC, but also those desmosomes at the umbrella cell:intermediate cell junction. The latter would ensure overall urothelial cohesion by strongly adhering umbrella cells to subjacent intermediate cells. We further observe that the keratin ovals are held together by struts formed from straight-appearing keratin filaments that cross the ovals at ~90° angles. This organization is consistent with a cell reacting to forces generated along its entire perimeter as the bladder fills. We further observed that the apical pole of umbrella cell nuclei are integrated into this girded layer, with close apposition of keratin filaments with the nuclear ectocytoskeleton. This may indicate a mechanism to convey cell-associated changes in cell shape and mechanical stress to the nucleus. The girded layer becomes more prominent when the bladder is filled to capacity, additional evidence that this structure likely plays an important role in maintaining umbrella cell cohesion during filling. Furthermore, the girded layer is largely absent in the umbrella cells of quiescent bladders. Thus, umbrella cells can rapidly adapt to a changing mechanical environment by altering the organization of its keratin network in response to filling, and then rapidly reverse these changes upon voiding.

SUMMARY

Epithelial cells must maintain a cohesive barrier in the face of mechanical forces such as when the skin is stretched, the lungs fill with air, food passes through the gut, or as the bladder fills with urine. In the case of umbrella cells, previous studies revealed mechanisms that contribute to tissue continuity during bladder filling including cell shape changes, surface area changes, and expansion of the tight and adherens junction (Truschel *et al.*, 2002; Eaton *et al.*, 2019; Dalghi *et al.*, 2020). Our current studies reveal that the umbrella cell keratin network, organized in part as a tile-like mesh, has several features that would contribute to umbrella cell mechanical stability including stretching and/or growing their keratin network, expanding the AJC-associated desmosomal necklace, and by forming a girded layer in response to filling, changes which are rapidly reversed upon voiding. Interestingly, a small subset of patients with the rare inherited skin disorder epidermolysis bullosa (which has multiple variants) suffer from mucosal defects of their internal organs including the bladder (Pearson, 1988; Fine *et al.*, 2004; Srinivasin and Palmer, 2007). The affected genes that give rise to epidermal bullosa include those encoding components of the basement membrane and hemidesmosomes (found in the basal layer of the urothelium), as well as PLEC and KRT5 and KRT14, keratins that are expressed by the basal and intermediate cell layers of the urothelium (Dalghi *et al.*, 2020; Has *et al.*, 2020). This is further evidence of the likely importance of the keratin cytoskeleton in urothelial stability and function.

MATERIALS AND METHODS

Request a protocol through *Bio-protocol*

Animals

Female Sprague-Dawley rats, 10–11 wk old (225–250 g in weight), were obtained from Inotiv-Envigo (West Lafayette, IN). They were housed, 2 animals per cage, in solid-bottom plastic cages. They were maintained under a 12-h day/night cycle and were fed standard rat chow and given water ad libitum. Female C57Bl6/J mice, 8–10 wk in age, were obtained from the Jackson Laboratory (Bar Harbor, ME). Mice were group housed (up to 5 mice/cage) in solid-bottom plastic cages under a 12-h day/night cycle. They were fed standard mouse chow and given water ad libitum. Animal studies were performed in accordance with relevant guidelines/regulations

of the Public Health Service Policy on Humane Care and Use of Laboratory Animals and the Animal Welfare Act, and under the approval of the University of Pittsburgh Institutional Animal Care and Use Committee (protocol numbers 24034669 and 22091937). Rats and mice were killed by CO_2 inhalation, followed by thoracotomy as a secondary method.

Reagents and antibodies

Unless specified otherwise, all chemicals were obtained from Sigma-Aldrich (St. Louis, MO). The source of primary and secondary antibodies used in this study is detailed in Table 1. Rhodamine-labeled phalloidin and DAPI were obtained from Molecular Probes (Thermo Fisher Scientific, Grand Island, NY) and Phalloidin-405 from Abcam (Waltham, MA).

Preparation of stretched bladders, filled bladders, voided bladders, and quiescent bladders

Stretched bladders were prepared as follows. Rats were euthanized and an incision was made along the ventral caudal midline, the bladder was exposed, clamped at the neck region (i.e., adjacent to the urethra) using a hemostat, and then excised. The bladder was carefully cut open along its midline from neck to dome using sharp surgical scissors and then rinsed in Krebs buffer (110 mM NaCl, 25 mM $NaHCO_3$, 5.8 mM KCl, 1.2 mM $MgSO_4$, 4.8 mM KH_2PO_4, 11 mM glucose, 2 mM $CaCl_2$, gassed with 5% vol/vol CO_2). The cut-open bladder was submerged in Krebs buffer and then pinned out on a rubber mat forming a 2 × 2 cm square. The tissue was then allowed to recover for 30 min in a tissue culture incubator held at 37°C and gassed with 5% vol/vol CO_2/95% vol/vol air. The tissue was then drug treated, extracted, and/or fixed as described below. SEM confirmed that tissue prepared in this manner was smooth and flat (i.e., lacked any rugae/large surface folds), the umbrella cells were polyhedral and not obviously pulled in one direction, and the tissue was morphologically similar to that observed when bladders are filled to 0.5 ml and then perfusion fixed.

Filled, voided, and quiescent bladders were prepared using our previously described techniques (Eaton *et al.*, 2019). Rats were anesthetized using 3% vol/vol isoflurane and then injected in their dorsal neck scruff subcutaneously with 1.4 g/kg urethane prepared fresh in dH_2O and sterile filtered through a 0.22-µm STERIFLIP-GP filter (Millipore Sigma) prior to use. The isoflurane was maintained for 5 min and then stopped. The animals were allowed to reach proper anesthetic depth over a period of ∼0.5–1.0 h, which was confirmed by lack of a response to a toe pinch. The animals were catheterized by inserting a 22-g Jelco IV catheter (Smiths-Medical, Minneapolis, MN) into the urethra and the animals were subjected to Credé's maneuver to void their bladders prior to the start of the experiment. Subsequently, animals in the filled and voided groups had their catheter ports closed, and their bladders were filled over 30 min to a final volume of 500–1000 µl using a Harvard Apparatus (Holliston, MA) PHD ultra syringe pump. Animals in the voided group had their catheter ports reopened and then allowed to void for 5 min. The animals with quiescent bladders remained catheterized, and their catheter ports were left open for the full 30-min period, maintaining their bladders in an empty state. At the end of the experiment, animals were perfusion fixed using the following methods. A thoracotomy was performed, the caudal vena cava was cut, and 50 ml of 100 mM Sorensen's phosphate buffer, pH 7.4 (phosphate buffer) at 37°C was perfused through the left ventricle using an 18-g needle. Subsequently, the perfusate was switched to phosphate buffer containing 4% wt/vol paraformaldehyde. The bladders were excised, placed in phosphate buffer containing 4% wt/vol paraformaldehyde, cut open down their midline and pinned out on a rubber mat, with minimal stretching, to expose the apical-most umbrella cell layer. The tissues were stored at 4°C in 1% wt/vol paraformaldehyde in phosphate buffer until ready for processing.

Thin-section TEM

Stretched bladders were fixed for 60 min at room temperature in 2.0% vol/vol glutaraldehyde (EMS; Electron Microscopy Sciences, Hatfield, PA), 4% vol/vol EM-grade paraformaldehyde in phosphate buffer. Alternatively, we used immunolabeled PREM samples, prepared as described below. The fixed tissues were cut into 1–2 mm^2 tissue blocks, rinsed with 100 mM cacodylate, pH 7.4 buffer and then osmicated in reduced 1.0% wt/vol OsO_4 (EMS) containing 1.5% wt/vol $K_4Fe(CN)_6$ and dissolved in 100 mM cacodylate buffer, pH 7.4 for 60 min at room temperature. The tissue blocks were rinsed three times with water and *en bloc* stained overnight at 4°C with an aqueous solution of 0.5% wt/vol uranyl acetate (EMS). The tissue blocks were dehydrated in ethanol, incubated in a 1:1 mixture of propylene oxide:LX112 epon substitute (Ladd Research, Essex Junction, VT) overnight, and then three changes of LX112 medium over the next 2 d, prior to embedding in flat rectangular silicone molds (Ladd Research) filled with LX112 medium. Samples were cured for 48 h at 60°C, the blocks were trimmed, and the tissue sectioned at 70 nm using a Leica Microsystems Ultracut R ultramicrotome (Wetzlar, Germany) outfitted with a Diatome Ultra 45° diamond knife (EMS-Diatome, Hatfield, PA). Sections, collected on Butvar-coated nickel grids, were contrasted with uranyl acetate and lead citrate (EMS) and viewed and photographed using a JEM1400 FLASH electron microscope (JEOL, Peabody, MA).

Cryosectioning of bladder tissue

Fixed, filled, and quiescent bladders were placed dome side down in cryomolds (15 × 15 × 5 mm; Thermo Fisher Scientific) filled with Optimal Cutting Temperature (OCT) solution (Tissue-Tek, Sakura Finetek, Torrance, CA), and flash frozen by placing the cryomold on a pool of liquid nitrogen. The blocks were stored at −80°C in tightly sealed plastic bags. Cryosections were cut using a CM1950 cryostat (Leica Microsystems, Buffalo Grove, IL; 8–12 µm sections; −20°C chamber and −18°C knife temperatures), collected on Superfrost Plus glass slides (Thermo Fisher Scientific), and held within the cryochamber at −20°C prior to immunolabeling or stored at −80°C.

Processing and immunolabeling of whole-mounted and cryosectioned bladder tissue

Stretched bladder tissue was prepared as described above and then fixed with 4% wt/vol paraformaldehyde in phosphate buffer for 30 min. The tissue was washed three times with PBS for 5 min and unreacted paraformaldehyde quenched using PBS containing 0.1% vol/vol Triton X-100, 20 mM glycine, pH 8.0, and 75 mM NH_4Cl_2. The tissue was rinsed with PEM buffer (100 mM PIPES, pH 6.9, 1 mM $MgCl_2$, 1 mM ethylene glycol tetraacetic acid [EGTA]) three times and then treated with Permeabilization and Cytoskeletal Stabilization (PCS) buffer, which was optimized for PREM (see below), and which is comprised of 100 mM PIPES, pH 6.9 (titrated with KOH), 1 mM $MgCl_2$, 1 mM EGTA, 5% vol/vol poly(ethylene glycol) octyl ether detergent (POE; stored under nitrogen), and 0.2% wt/vol polyethylene glycol (20,000 mwt; Thermo Fisher Scientific) for 45 min at room temperature on a slowly-rotating orbital shaker (30 rpm). The tissue was then rinsed with PEM buffer three times.

Target	Name	Source and catalogue number	Host	Species reactivity (according to manufacturer)	Application (Dilution)
		Primary antibodies			
CDH1	E-cadherin	BD Transduction labs (610181)	Mouse	Human (QC Testing), Mouse, Rat, Dog (Tested in Development)	IF (1:100)
CLDN8	Claudin-8	Invitrogen (400700Z)	Rabbit	Dog, Mouse, Rat	IF (1:100)
DSC2	Desmocollin-2	Biotechne/Novus (NB25337820/AF7490-SP)	Sheep	Mouse	IF (1:100)
DSG2	Desmoglein-2	Novus (NBP133374)	Rabbit	Human, Mouse	IF (1:100)
DSP	Desmoplakin	Progen (DP-1)	Guinea pig	Bovine, Human	IF (1:100)
KRT8	Keratin-8	Developmental Studied Hybridoma Bank (clone TROMA-1)	Rat	Canine, Human, Mouse	IF (1:100)
KRT8	Keratin-8	Abcam (ab59400)	Rabbit	Human	IF (1:100)
KRT20	Keratin-20	Dako (M7019)	Mouse	Human	IF (1:100)
KRT20	Keratin-20	Abcam (ab53120)	Rabbit	Human	IF (1:100)
MYH1	Myosin heavy chain I (N-terminus)	ThermoFisher (25182-1-AP)	Rabbit	Human, Mouse	IF (1:200)
PLEC	Plectin	Progen (GP21)	Guinea pig	Bovine, Human, Mouse	IF (1:100)
TJP1	ZO-1	Invitrogen (617300)	Rabbit	Dog, Guinea pig, Human, Mouse, Rat	IF (1:100) EM (1:25)
TUB1A1	Alpha-tubulin	Sigma (T9026) (clone is DM1A) ascites	Mouse	yeast, mouse, amphibian, human, rat, chicken, fungi, bovine	IF (1:500)
		Secondary antibodies			
Target	Conjugates and catalogue number	Source	Host species	Species reactivity	Application
Guinea Pig IgG (H+L)	Alexa 488 (#706-165-148) Cy3 (#706-545-148) Cy5 (#706-175-148)	Jackson ImmunoResearch	Donkey	Guinea pig (min X Bovine, Chicken, Goat, Syrian Hamster, Horse, Human, Mouse, Rabbit, Rat, Sheep Serum Proteins	IF Alexa 488 (1:100) IF Cy3 (1:3000) IF Cy5 (1:100)
Rat IgG (H+L)	Dylight 405 (#712-475-150)	Jackson ImmunoResearch	Donkey	Rat (min X Bovine, Chicken, Goat, Guinea Pig, Syrian Hamster, Horse, Human, Rabbit, Sheep Serum Proteins)	IF (1:100)
Rabbit IgG (H+L)	Alexa 488 (#711-545-152) Cy3 (#711-165-152) Cy5 (#711-605-152)	Jackson ImmunoResearch	Donkey	Rabbit (min X Bovine, Chicken, Goat, Guinea Pig, Syrian Hamster, Horse, Human, Mouse, Rat, Sheep Serum Proteins)	IF Alexa 488 (1:100) IF Cy3 (1:3000) IF Cy5 (1:100)
Rabbit IgG (H+L)	Cy3 (#111-025-045)	Jackson ImmunoResearch	Goat	Rabbit (min X human serum proteins)	IF (1:3000)
Rat IgG (H+L)	Cy3 (#712-165-153)	Jackson ImmunoResearch	Donkey	Rat (min X Bovine, Chicken, Goat, Guinea Pig, Syrian Hamster, Horse, Human, Mouse, Rabbit, Sheep Serum Proteins)	IF (1:3000)
Sheep IgG (H+L)	Cy3 (#713-165-147)	Jackson ImmunoResearch	Donkey	Mouse (min X Chicken, Guinea Pig, Syrian Hamster, Horse, Human, Mouse, Rabbit, Rat, Sheep Serum Proteins)	IF Cy3 (1:3000)
Mouse IgG (H+L)	Alexa 488 (#715-545-151) Alexa 647 (#715-605-151)	Jackson ImmunoResearch	Donkey	Mouse (min X Bovine, Chicken, Goat, Guinea Pig, Syrian Hamster, Horse, Human, Rabbit, Rat, Sheep Serum Proteins)	IF Alexa 488 (1:100) IF Alexa 647 (1:100)
Rat IgG (H+L)	12 nm gold (112-205-167)	Jackson ImmunoResearch	Goat	Rat (min X human, bovine, horse, mouse, rabbit serum proteins)	EM (1:10)

TABLE 1: Antibodies used in this study.

Immunofluorescence labeling of whole-mounted (stretched, filled, quiescent, voided) and cryosectioned bladder tissue was performed at room temperature, unless otherwise indicated. For cryosectioned tissue, the slide-mounted sections were washed three times with PBS for 5 min and unreacted paraformaldehyde quenched using PBS containing 0.1% (vol/vol) Triton X-100, 20 mM glycine, pH 8.0, and 75 mM ammonium chloride. The procedure for whole-mounted or cryosectioned tissue was similar. Samples were washed three times with PBS for 5 min, and then three times quickly with Block Solution (which contained 0.7% wt/vol fish-skin gelatin, 0.025% wt/vol saponin, and 0.02% wt/vol sodium azide, all dissolved in PBS). The tissue was then incubated for 30 min in Block Solution supplemented with 5% vol/vol donkey serum, and then incubated overnight at 4°C in Block Solution containing a mixture of primary antibodies. Subsequently, the tissue was washed three times quickly with Block Solution, and then three times for 5 min with Block Solution prior to incubating the tissue with secondary antibodies, diluted in Block Solution, for 1 h. Tissue was then washed three times quickly with Block Solution, three times for 5 min with Block Solution, and then three times with PBS. The samples were postfixed with 4% (wt/vol) paraformaldehyde dissolved in phosphate buffer for 10 min (tissue sections) or 20 min (whole-mount), after which the tissue was washed three times with PBS. After labeling, cryosections were covered with a drop of Slowfade Diamond Antifade mountant (refractive index of 1.42; Thermo Fisher Scientific), covered with a Gold Seal Cover Glass (number 1.5, Thermo Fisher Scientific), and sealed around the edges with a thin layer of clear nail polish (EMS). Whole-mount tissue was placed, mucosal surface facing up, within a square well created with nail polish in which a drop of Slowfade Diamond Antifade Mountant was added. An additional drop of mountant was added to the top of the tissue. A cover glass was placed over the tissue and sealed around its edges with a thin layer of nail polish. Samples were stored at −20°C. Use of Slowfade-Glass antifade mountant (Thermo Fisher Scientific), which has a refractive index of 1.52, did not significantly enhance our image quality and was not routinely employed.

Image acquisition, 3D image reconstruction, and video production

Images were captured by confocal microscopy using a Leica DMI8 microscope and either a Leica HC PL APO CS2 10X, 0.4NA dry objective, a Leica HC PL APO CS2 40X, 1.30NA oil objective, a Leica HC PL APO CS2 63X, 1.4NA oil objective, or a 100X HC PL APO, 1.4 NA oil objective and the appropriate laser lines of a Leica Microsystems SP8 Stellaris confocal system outfitted with a 405-nm laser diode and a white-light laser. The signal from the HyDS and HyDX detectors was optimized using the Q-LUT option and crosstalk between channels was prevented by use of spectral detection coupled with sequential scanning. For standard confocal microscopy, 8-bit images (1024 × 1024) were collected at 600 Hz using 3-line averages, with a pinhole diameter of 1.0Airy unit, and system-optimized parameters for the *Z*-axis. For SRIP-confocal microscopy we used the LIGHTNING deconvolution processing module set to its highest quality setting. Images (16 bit), captured using a pinhole set to 0.5Airy units, were collected using system optimized settings for image dimensions and Z-section thickness. The resulting images had X and Y pixel sizes in the range of 30–40 nm and Z sizes in the range of 135–500 nm depending on lens/zoom combinations. Images were processed using Imaris software v10.1 (Oxford Instruments, Boston, MA), employing the 3D-visualization option along with surface segmentation, classifier subsegmentation routines, and slicers as required. Image intensity was corrected in Imaris, and image files were exported as TIFF files. Composite images were prepared in Adobe Illustrator CC2024. Videos were generated using the Animation tools provided in the Imaris software package. Movies were compressed using Handbrake software (available at handbrake.fr). Images are representative of experiments performed in 5–10 rats.

Quantitation of desmosome parameters in filled and voided bladders

The Navigator function of Leica LASX software, in conjunction with the 10X objective (zoom set to 1.0), was employed to generate images of entire filled and voided rat bladders immunolabeled with antibodies to DSG2 and stained with phalloidin as a marker of the AJC-associated actin ring (and lateral cell surface). The Navigator tool was used to superimpose a grid on the image (each square encompassing an area of ∼1165 × 1165 µm) and a random number table was used to identify 10 areas for further analysis. Z-stacks, obtained from the center of each of these 10 areas, were collected (63X objective, zoom = 1, ∼185 × 185 µm area) using the LIGHTNING deconvolution module described above. If multiple whole cells were present in an image, a random number table was used to identify cells for further analysis. The Z-stacks were imported into Imaris, and the "Surfaces tool" of the 3D visualization module was used to segment the DSG2-labeled desmosomes. Actin staining, along with tilting/rotating of the 3D image, was used to identify desmosomes associated with the AJC versus those along the lateral membrane, or at the umbrella cell:intermediate cell interface. The Classification option was then used to select the AJC-associated desmosomes and the following parameters were determined: total number, as well as the individual area and volume for each identified desmosome. The total number of classified objects is displayed in the classifier window, while the latter two parameters were found in the "Statistics > Detailed" tabs. Information for each desmosome was exported to Excel (Microsoft, Seattle, WA) and mean values for each sample area, and then for each animal bladder were calculated. The mean ± SEM of the composite data for each treatment group ($n = 4$) are reported. In addition, the Imaris Filament tool was used in conjunction with the AJC-associated actin and DSG2 labeling to define and quantify the cell perimeter. Values for each animal were averaged and the mean ± SEM of the composite data reported.

PREM and SEM

PREM was performed using a previously described protocol (Svitkina, 2016), but with the following modifications. The original protocol calls for the use of Triton X-100 to remove membranes, but the umbrella cell apical membrane is highly detergent resistant and is not solubilized by Triton-X-100 (Liang *et al.*, 1999). We also found that octylglucoside and digitonin were also ineffective. In contrast, the nonionic detergent POE effectively removed membrane while preserving the cytoskeleton. An additional, key modification to the published PREM protocol included reducing the concentration of polyethylene glycol, a cytoskeleton stabilizing agent, in the extraction solution from 2.0–0.2%. At the higher concentration, a large amount of residual protein adhered to the cytoskeleton, obscuring its visualization. The lower concentration effectively maintained the cytoskeletal architecture while eliminating much (but not all) of the adherent protein.

In our studies, we used unfixed and stretched bladder tissue, prepared as described above. The tissue was rinsed with PBS and then treated with freshly prepared PCS buffer supplemented with

2 μM unlabeled phalloidin for 45 min at room temperature on a slowly rotating orbital shaker (30 rpm). The tissue was rinsed with PEM buffer three times, rotating the dish by hand after each wash. The sample was then treated for 30 min at room temperature with 1 mg/ml S1 fragments derived from rabbit psoas skeletal muscle (Cytoskeleton Incorporated, Denver, CO; CS-MYS04), reconstituted in PEM buffer containing 2.0 μM phalloidin and centrifuged at 100,000 × *g* for 15 min at 4°C prior to use. The tissue was then rinsed with PEM buffer, then PBS, and then fixed in 2% vol/vol glutaraldehyde in phosphate buffer for 30 min at room temperature. The tissue was then rinsed with distilled water, treated with an aqueous 0.1% wt/vol solution of tannic acid (EMS) for 20 min, rinsed twice with distilled H_2O, washed with distilled H_2O for 5 min, treated with 0.2% wt/vol aqueous uranyl acetate for 20 min at room temperature, and then dehydrated using ethanol. The sample was then treated with 0.2% wt/vol uranyl acetate (prepared in ethanol) for 20 min at room temperature, and then dehydrated further using 100% ethanol for 5 min, followed by two 5-min incubations with molecular-sieve–dried ethanol (prepared as described [Svitkina, 2016]). The samples were then critical point dried using a Samdri-PVT-3D critical point dryer (Tousimis, Rockville, MD) fed with bone-dry CO_2. For PREM, the dried samples were transferred to a JEOL JFD-V-TP device, rotary shadowed with ∼2 nm of platinum at 45°, followed by shadowing with ∼5.0 nm of carbon. As household bleach was generally ineffective at removing residual tissues from replicas, they were instead treated with a 1:10 dilution of sodium hypochlorite (4.0–4.99% available chloride) overnight at room temperature in porcelain spot plates to remove remaining tissue. The replicas were washed with H_2O three times and then picked up on Butvar-coated nickel grids and viewed in a JEOL1400 FLASH TEM. For SEM, the critical point dried samples (taken prior to rotary shadowing) were sputter coated with gold palladium using a Cressington 108auto sputter coater (Ted Pella, Redding, CA), mounted on aluminum stubs, and viewed in a JEOL 6335F field-emission SEM. Immunogold labeling was performed as described by Svitkina *et al.* (Svitkina, 2016). The PREM and SEM images presented are representative of experiments performed on 5–10 rats.

Treatment with CytoD, LatA, nocodazole, and plecstatin-1

Stretched bladder tissue was prepared as described above. After the 30-min equilibration in Krebs buffer, the tissue was treated for 60 min at 37°C with 33 μM nocodazole, 25 μg/ml CytoD, 1–50 μM LatA (Biotechne Tocris Bioscience, Minneapolis, MN), 25 μM plecstatin-1-HCl (MedChemExpress, Monmouth Junction, NJ), or DMSO dissolved in Krebs buffer. All drugs were prepared as 1000-fold stock solutions, stored as aliquots at −20°C, and diluted just prior to use.

Detection of PLEC variants in rodent umbrella cells using PCR

For mouse urothelium, the following protocol was employed. Mouse bladders were excised and rinsed with Kreb's buffer. The pointed end of a yellow tip, trimmed by 5 mm with a scalpel, was positioned next to the dome of the bladder. Fine forceps were used to invert the bladder onto the tip (mucosal surface now facing out). The inverted bladder was placed in 150 μl of lysis/binding buffer (RNAqueous-4PCR Kit; Invitrogen, Waltham, MA) for 30 s and total RNA was isolated per the manufacturer's protocol. An AccuScript PfuUltra II RT-PCR kit (Agilent, Santa Clara, CA) was used to generate cDNAs using random primers and following the manufacturer's protocol. The splice variant-specific primers employed for PCR analysis were those provided by Rezniczek *et al* (Rezniczek *et al.*, 2016). PCR reactions, were performed using the KAPA HiFi polymerase kit (Roche Sequencing Solutions, Pleasanton, CA) and a T100 Thermal Cycler (Bio-Rad, Hercules, CA) using the following protocol: initial denaturation at 94°C for 2 min, followed by 39 cycles of 94°C for 20 s, 60°C for 15 s, 72°C for 15 s, and a final step of 72°C for 2 min prior to holding at 4°C. Amplicons were resolved using 2% wt/vol agarose gels.

For rat umbrella cells, the following protocol was performed. Stretched rat bladders were pinned out on rubber mats and treated with 2.5 mg/ml Dispase (Life Technologies-Thermo Fisher Scientific) dissolved in Minimal Essential Medium (Life Technologies-Thermo Fisher Scientific) for 60 min at 37°C in a cell culture incubator. The mucosal surface was gently scraped using blunt forceps, and the medium with cells collected and centrifuged at 200 × *g* in a table-top centrifuge for 5 min. The cell pellet was resuspended in Kreb's buffer, and while viewing through a microscope an oil-filled glass pipette (prepared from borosilicate glass capillary tubes using a PP-81 puller; Narishige International USA, Amityville, NY), attached to a Nanoject II suction system (Drummond Scientific, Broomall, PA), was used to collect a total of 30 umbrella cells. The latter were identified by their large size and binucleate morphology. Cell lysis and cDNA synthesis was performed using the SuperScript IV CellsDirect cDNA Synthesis kit (Thermo Fisher Scientific). PCR was performed as described above, but using the following primers:

RAT-Plec1-Fwr: TGACCTCGCTGAAAGCTCG
RAT-Plec1-Rev: GGTCTCGTTCATCTGTGGCT
RAT-Plec1a-Fwr: GGTAGCAAGAGAACCAGCTCA
RAT-Plec1a-Rev: AGGTGTTTATTGACCCACTTG
RAT-Plec1c-Fwr: GAGTGGAGGTGGTTCTGTGG
RAT-Plec1c-Rev: AGGTGTTTATTGACCCACTTG
RAT-Plec1f-Fwr: CCGACGAACAGGACTTCATC
RAT-Plec1f-Rev: AGGTGTTTATTGACCCACTTG

Generation of PLEC1-8-EGFP and PLEC1a6-8-EGFP adenoviruses and in-situ adenoviral transduction

Gene synthesis, subcloning into adenoviral expression vectors, and adenovirus production of the PLEC1a-8-EGFP and PLEC1a6-8-EGFP constructs was performed by VectorBuilder (Chicago, IL). For the PLEC1a-8-EGFP construct, a cDNA was synthesized that encoded amino acids 1–275 of the rat PLEC1a variant (transcript variant 11, NCBI Reference Sequence: NM_001164308.3; exons 1–8), followed by the in-frame addition of a 5′-ggcagcgcgggcagcgcggcgggcagcggcgaattt sequence (encoding a GSAGSAAGSGEF flexible linker) and the cDNA sequence encoding EGFP. The PLEC1a6-8-EGFP construct was identical but lacked exons 2–5 (which encode amino acids 38–151), generating a construct that lacked the calponin-homology domain1 actin binding motif of PLEC1a. The synthesized constructs, with included Kozak sequences, were cloned into the pAVexpression vector behind a CMV promoter and adenoviruses were produced using the pilot-scale packaging service. Upon receipt, the adenoviruses were further amplified using our previously described methods and stored at −80°C prior to use (Ruiz *et al.*, 2022).

In situ transduction was performed as described previously (Khandelwal *et al.*, 2008; Ruiz *et al.*, 2022). Note that transduced cells maintain expression of differentiation markers such as uroplakins and achieve a high transepithelial resistance; however, they only have a single nucleus (Khandelwal *et al.*, 2008; Eaton *et al.*, 2019). The latter is a function of detergent treatment and not a response to viral transduction *per se*. Briefly, mice were sedated with

2.5% (vol/vol) isoflurane and a 22-g Jelco IV catheter, with Luer fitting (Smith Medicals) and trimmed to ~1 cm in length, was inserted into the bladder via the urethra. The bladder was rinsed with 100 µl of PBS delivered via a 1-ml syringe, which was then detached to allow the buffer to void. The bladder was then filled with 100 µl of 0.1% wt/vol dodecyl-β-D-maltoside dissolved in PBS via syringe. The syringe was left attached to the catheter for 10 min to prevent the solution from escaping. The bladder was allowed to void, and then was filled with 100 µl PBS via syringe containing adenoviruses expressing the constructs described above (1.0×10^8 infectious virus particles per animal). The syringe was left in place, and after 30 min detached and the virus solution was allowed to void. Anesthesia was discontinued, and the mice were allowed to revive. At 48–h posttransduction, the mice were subjected to the filled bladder protocol described above with the following changes. Mice were anesthetized with 2.5% vol/vol isoflurane and the mouse bladders were filled to 150 µl over 30 min prior to perfusion fixation. Samples were processed for immunofluorescence as described above.

Quantitation of plecstatin-1–induced foci

Stretched bladder tissue was treated with 25 µM plecstatin-1 or DMSO solvent for 60 min at 37°C, fixed in 4.0% wt/vol paraformaldehyde in 0.1M phosphate buffer, and processed for immunofluorescence using phalloidin and antibodies to PLEC and the methods described above. Six random Z-stacks were collected from each of three bladders per treatment group using the confocal microscope setup described above with a 40X objective and with a zoom set to 1X. The number of $PLEC^+$ $phalloidin^+$ foci were counted in each image, normalized to mm^2, and the mean ± SEM determined.

Statistical analysis

Data are reported as mean ± SEM. Data were analyzed using Prism10 software (Graphpad, La Jolla, CA). After confirming normality using a Kolmogorov–Smirnov test, statistically significant differences were determined using unpaired, two-tailed Student *t* tests with Welch's correction for unequal variance. A p value ≤ 0.05 was taken as being statistically significant.

ACKNOWLEDGMENTS

This work was supported by grants from the National institutes of Health, including R01DK129473 (to G.A.) and by the Pittsburgh Center for Kidney Research KIDNIT resource development imaging core (U54DK137329). The Leica Stellaris confocal used in this study was funded by S10OD028596 (to G.A.).

REFERENCES

Ameen NA, Figueroa Y, Salas PJ (2001). Anomalous apical plasma membrane phenotype in CK8-deficient mice indicates a novel role for intermediate filaments in the polarization of simple epithelia. J Cell Sci 114, 563–575.

Andra K, Nikolic B, Stocher M, Drenckhahn D, Wiche G (1998). Not just scaffolding: Plectin regulates actin dynamics in cultured cells. Genes Dev 12, 3442–3451.

Ao X, Lehrer SS (1995). Phalloidin unzips nebulin from thin filaments in skeletal myofibrils. J Cell Sci 108, 3397–3403.

Baddam SR, Arsenovic PT, Narayanan V, Duggan NR, Mayer CR, Newman ST, Abutaleb DA, Mohan A, Kowalczyk AP, Conway DE (2018). The desmosomal cadherin desmoglein-2 experiences mechanical tension as demonstrated by a FRET-based tension biosensor expressed in living cells. Cells 7, 66.

Bharathan NK, Mattheyses AL, Kowalczyk AP (2024). The desmosome comes into focus. J Cell Biol 223, e202404120.

Burdett ID (1993). Internalisation of desmosomes and their entry into the endocytic pathway via late endosomes in MDCK cells. Possible mechanisms for the modulation of cell adhesion by desmosomes during development. J Cell Sci 106, 1115–1130.

Carattino MD, Prakasam HS, Ruiz WG, Clayton DR, McGuire M, Gallo LI, Apodaca G (2013). Bladder filling and voiding affect umbrella cell tight junction organization and function. Am J Physiol Renal Physiol 305, F1158–F1168.

Castanon MJ, Walko G, Winter L, Wiche G (2013). Plectin-intermediate filament partnership in skin, skeletal muscle, and peripheral nerve. Histochem Cell Biol 140, 33–53.

Chen J, Nekrasova OE, Patel DM, Klessner JL, Godsel LM, Koetsier JL, Amargo EV, Desai BV, Green KJ (2012). The C-terminal unique region of desmoglein 2 inhibits its internalization via tail-tail interactions. J Cell Biol 199, 699–711.

Coch RA, Leube RE (2016). Intermediate filaments and polarization in the intestinal epithelium. Cells 5, 32.

Dalghi MG, Montalbetti N, Carattino MD, Apodaca G (2020). The Urothelium: Life in a liquid environment. Physiol Rev 100, 1621–1705.

Demlehner MP, Schafer S, Grund C, Franke WW (1995). Continual assembly of half-desmosomal structures in the absence of cell contacts and their frustrated endocytosis: A coordinated Sisyphus cycle. J Cell Biol 131, 745–760.

Eaton AF, Clayton DR, Ruiz WG, Griffiths SE, Rubio ME, Apodaca G (2019). Expansion and contraction of the umbrella cell apical junctional ring in response to bladder filling and voiding. Mol Biol Cell 30, 2037–2052.

Farquhar MG, Palade GE (1963). Junctional complexes in various epithelia. J Cell Biol 17, 375–412.

Fine JD, Johnson LB, Weiner M, Stein A, Cash S, DeLeoz J, Devries DT, Suchindran C (2004). Genitourinary complications of inherited epidermolysis bullosa: experience of the national epidermylosis bullosa registry and review of the literature. J Urol 172, 2040–2044.

Foisner R, Bohn W, Mannweiler K, Wiche G (1995). Distribution and ultrastructure of plectin arrays in subclones of rat glioma C6 cells differing in intermediate filament protein (vimentin) expression. J Struct Biol 115, 304–317.

Foisner R, Wiche G (1987). Structure and hydrodynamic properties of plectin molecules. J Mol Biol 198, 515–531.

Fontao L, Geerts D, Kuikman I, Koster J, Kramer D, Sonnenberg A (2001). The interaction of plectin with actin: Evidence for cross-linking of actin filaments by dimerization of the actin-binding domain of plectin. J Cell Sci 114, 2065–2076.

Fuchs P, Zorer M, Rezniczek GA, Spazierer D, Oehler S, Castanon MJ, Hauptmann R, Wiche G (1999). Unusual 5′ transcript complexity of plectin isoforms: novel tissue-specific exons modulate actin binding activity. Hum Mol Genet 8, 2461–2472.

Fudge D, Russell D, Beriault D, Moore W, Lane EB, Vogl AW (2008). The intermediate filament network in cultured human keratinocytes is remarkably extensible and resilient. PLoS One 3, e2327.

Gallo LI, Dalghi MG, Clayton DR, Ruiz WG, Khandelwal P, Apodaca G (2018). RAB27B requirement for stretch-induced exocytosis in bladder umbrella cells. Am J Physiol Cell Physiol 314, C349–C365.

Gittes F, Mickey B, Nettleton J, Howard J (1993). Flexural rigidity of microtubules and actin filaments measured from thermal fluctuations in shape. J Cell Biol 120, 923–934.

Glotfelty LG, Zahs A, Iancu C, Shen L, Hecht GA (2014). Microtubules are required for efficient epithelial tight junction homeostasis and restoration. Am J Physiol Cell Physiol 307, C245–C254.

Gov NS (2007). Active elastic network: cytoskeleton of the red blood cell. Phys Rev E Stat Nonlin Soft Matter Phys 75, 011921.

Has C, Bauer JW, Bodemer C, Bolling MC, Bruckner-Tuderman L, Diem A, Fine JD, Heagerty A, Hovnanian A, Marinkovich MP, *et al.* (2020). Consensus reclassification of inherited epidermolysis bullosa and other disorders with skin fragility. Br J Dermatol 183, 614–627.

Hegazy M, Perl AL, Svoboda SA, Green KJ (2022). Desmosomal cadherins in health and disease. Annu Rev Pathol 17, 47–72.

Hatzfeld M, Keil R, Magin TM (2017). Desmosomes and Intermediate Filaments: Their Consequences for Tissue Mechanics. Cold Spring Harb Perspect Biol 9, a029157 10.1101/cshperspect.a029157.

Hicks M (1975). The mammalian urinary bladder: an accommodating organ. Biol Rev Camb Philos Soc 50, 215–246.

Higashi T, Miller AL (2017). Tricellular junctions: How to build junctions at the TRICkiest points of epithelial cells. Mol Biol Cell 28, 2023–2034.

Hirokawa N, Tilney LG, Fujiwara K, Heuser JE (1982). Organization of actin, myosin, and intermediate filaments in the brush border of intestinal epithelial cells. J Cell Biol 94, 425–443.

Holm PK, Hansen SH, Sandvig K, van Deurs B (1993). Endocytosis of desmosomal plaques depends on intact actin filaments and leads to a non-degradative compartment. Eur J Cell Biol 62, 362–371.
Holthofer B, Windoffer R, Troyanovsky S, Leube RE (2007). Structure and function of desmosomes. Int Rev Cytol 264, 65–163.
Ishikawa H, Bischoff R, Holtzer H (1969). Formation of arrowhead complexes with heavy meromyosin in a variety of cell types. J Cell Biol 43, 312–328.
Ivaska J, Vuoriluoto K, Huovinen T, Izawa I, Inagaki M, Parker PJ (2005). PKCepsilon-mediated phosphorylation of vimentin controls integrin recycling and motility. EMBO J 24, 3834–3845.
Jacob JT, Coulombe PA, Kwan R, Omary MB (2018). Types I and II keratin intermediate filaments. Cold Spring Harb Perspect Biol 10, a018275.
Jirouskova M, Nepomucka K, Oyman-Eyrilmez G, Kalendova A, Havelkova H, Sarnova L, Chalupsky K, Schuster B, Benada O, Miksatkova P, *et al*. (2018). Plectin controls biliary tree architecture and stability in cholestasis. J Hepatol 68, 1006–1017.
Khandelwal P, Prakasam HS, Clayton DR, Ruiz WG, Gallo LI, van Roekel D, Lukianov S, Peranen J, Goldenring JR, Apodaca G (2013). A Rab11a-Rab8a-Myo5B network promotes stretch-regulated exocytosis in bladder umbrella cells. Mol Biol Cell 24, 1007–1019.
Khandelwal P, Ruiz G, Balestreire-Hawryluk E, Weisz OA, Goldenring JA, Apodaca G (2008). Rab11a-dependent exocytosis of discoidal/fusiform vesicles in bladder umbrella cells. Proc Natl Acad Sci USA 105, 15773–15778.
Khandelwal P, Ruiz WG, Apodaca G (2010). Compensatory endocytosis in bladder umbrella cells occurs through an integrin-regulated and RhoA- and dynamin-dependent pathway. EMBO J 29, 1961–1975.
Krausova A, Buresova P, Sarnova L, Oyman-Eyrilmez G, Skarda J, Wohl P, Bajer L, Sticova E, Bartonova L, Pacha J, *et al*. (2021). Plectin ensures intestinal epithelial integrity and protects colon against colitis. Mucosal Immunol 14, 691–702.
Kreplak L, Bar H, Leterrier JF, Herrmann H, Aebi U (2005). Exploring the mechanical behavior of single intermediate filaments. J Mol Biol 354, 569–577.
Latorre E, Kale S, Casares L, Gomez-Gonzalez M, Uroz M, Valon L, Nair RV, Garreta E, Montserrat N, Del Campo A, *et al*. (2018). Active superelasticity in three-dimensional epithelia of controlled shape. Nature 563, 203–208.
Lewis SA, de Moura JLC (1982). Incorporation of cytoplasmic vesicles into apical membrane of mammalian urinary bladder epthelium. Nature 297, 685–689.
Liang F, Kachar B, Ding M, Zhai Z, Wu X-R, Sun TT (1999). Urothelial hinge as a highly specialized membrane: Detergent-insolubility, urohingin association, and in vitro formation. Differentiation 65, 59–69.
Ma L, Xu J, Coulombe PA, Wirtz D (1999). Keratin filament suspensions show unique micromechanical properties. J Biol Chem 274, 19145–19151.
Margiotta A, Bucci C (2016). Role of intermediate filaments in vesicular traffic. Cells 5, 20.
McGough A, Pope B, Chiu W, Weeds A (1997). Cofilin changes the twist of F-actin: implications for actin filament dynamics and cellular function. J Cell Biol 138, 771–781.
McMillan JR, Shimizu H (2001). Desmosomes: Structure and function in normal and diseased epidermis. J Dermatol 28, 291–298.
Meier SM, Kreutz D, Winter L, Klose MHM, Cseh K, Weiss T, Bileck A, Alte B, Mader JC, Jana S, *et al*. (2017). An organoruthenium anticancer agent shows unexpected target selectivity for plectin. Angew Chem Int Ed Engl 56, 8267–8271.
Moch M, Schwarz N, Windoffer R, Leube RE (2020). The keratin-desmosome scaffold: pivotal role of desmosomes for keratin network morphogenesis. Cell Mol Life Sci 77, 543–558.
Mucke N, Kreplak L, Kirmse R, Wedig T, Herrmann H, Aebi U, Langowski J (2004). Assessing the flexibility of intermediate filaments by atomic force microscopy. J Mol Biol 335, 1241–1250.
Nikolic B, Mac Nulty E, Mir B, Wiche G (1996). Basic amino acid residue cluster within nuclear targeting sequence motif is essential for cytoplasmic plectin-vimentin network junctions. J Cell Biol 134, 1455–1467.
Oriolo AS, Wald FA, Ramsauer VP, Salas PJ (2007). Intermediate filaments: a role in epithelial polarity. Exp Cell Res 313, 2255–2264.
Pan X, Hobbs RP, Coulombe PA (2013). The expanding significance of keratin intermediate filaments in normal and diseased epithelia. Curr Opin Cell Biol 25, 47–56.
Pearson RW (1988). Clinicopathologic types of epidermolysis bullosa and their nondermatological complications. Arch Dermatol 124, 718–725.
Perrot R, Julien JP (2009). Real-time imaging reveals defects of fast axonal transport induced by disorganization of intermediate filaments. FASEB J 23, 3213–3225.
Picu RC (2011). Mechanics of random fiber networks - a review. Soft Matter 7, 6768–6785.
Potokar M, Stenovec M, Gabrijel M, Li L, Kreft M, Grilc S, Pekny M, Zorec R (2010). Intermediate filaments attenuate stimulation-dependent mobility of endosomes/lysosomes in astrocytes. Glia 58, 1208–1219.
Prechova M, Adamova Z, Schweizer AL, Maninova M, Bauer A, Kah D, Meier-Menches SM, Wiche G, Fabry B, Gregor M. (2022). Plectin-mediated cytoskeletal crosstalk controls cell tension and cohesion in epithelial sheets. J Cell Biol 221, e202105146.
Price AJ, Cost AL, Ungewiss H, Waschke J, Dunn AR, Grashoff C (2018). Mechanical loading of desmosomes depends on the magnitude and orientation of external stress. Nat Commun 9, 5284.
Quinlan RA, Schwarz N, Windoffer R, Richardson C, Hawkins T, Broussard JA, Green KJ, Leube RE (2017). A rim-and-spoke hypothesis to explain the biomechanical roles for cytoplasmic intermediate filament networks. J Cell Sci 130, 3437–3445.
Rezniczek GA, Winter L, Walko G, Wiche G (2016). Functional and genetic analysis of plectin in skin and muscle. Methods Enzymol 569, 235–259.
Rondanino C, Rojas R, Ruiz WG, Wang E, Hughey RP, Dunn KW, Apodaca G (2007). RhoB-dependent modulation of postendocytic traffic in polarized Madin-Darby canine kidney cells. Traffic 8, 932–949.
Ruiz WG, Clayton DR, Dalghi MG, Montalbetti N, Carattino MD, Apodaca G (2022). Expression of transgenes in native bladder urothelium using adenovirus-mediated transduction. J Vis Exp 188, 10.3791/64584.
Schwarz N, Leube RE (2023). Plasticity of cytoplasmic intermediate filament architecture determines cellular functions. Curr Opin Cell Biol 85, 102270.
Srinivasin A, Palmer LS (2007). Genitourinary complications of epidermolysis bullosa. Urology 70, 179.e175–176.
Stenvall CA, Nystrom JH, Butler-Hallissey C, Jansson T, Heikkila TRH, Adam SA, Foisner R, Goldman RD, Ridge KM, Toivola DM (2022). Cytoplasmic keratins couple with and maintain nuclear envelope integrity in colonic epithelial cells. Mol Biol Cell 33, ar121.
Svitkina T (2016). Imaging cytoskeleton components by electron microscopy. Methods Mol Biol 1365, 99–118.
Svitkina TM, Verkhovsky AB, Borisy GG (1996). Plectin sidearms mediate interaction of intermediate filaments with microtubules and other components of the cytoskeleton. J Cell Biol 135, 991–1007.
Szeverenyi I, Cassidy AJ, Chung CW, Lee BT, Common JE, Ogg SC, Chen H, Sim SY, Goh WL, Ng KW, *et al*. (2008). The Human Intermediate Filament Database: Comprehensive information on a gene family involved in many human diseases. Hum Mutat 29, 351–360.
Tateishi K, Nishida T, Inoue K, Tsukita S (2017). Three-dimensional organization of layered apical cytoskeletal networks associated with mouse airway tissue development. Sci Rep 7, 43783.
Terada N, Ohno N, Saitoh S, Saitoh Y, Fujii Y, Kondo T, Katoh R, Chan C, Abraham SN, Ohno S (2009). Involvement of dynamin-2 in formation of discoid vesicles in urinary bladder umbrella cells. Cell Tissue Res 337, 91–102.
Truschel ST, Wang E, Ruiz WG, Leung SM, Rojas R, Lavelle J, Zeidel M, Stoffer D, Apodaca G (2002). Stretch-regulated exocytosis/endocytosis in bladder umbrella cells. Mol Biol Cell 13, 830–846.
van Bodegraven EJ, Etienne-Manneville S (2021). Intermediate filaments from tissue integrity to single molecule mechanics. Cells 10, 1905.
Veranic P, Jezernik K (2002). Trajectorial organisation of cytokeratins within the subapical region of umbrella cells. Cell Motil Cytoskeleton 53, 317–325.
Wiche G (2021). Plectin-mediated intermediate filament functions: Why isoforms matter. Cells 10, 2154.
Wiche G, Krepler R, Artlieb U, Pytela R, Denk H (1983). Occurrence and immunolocalization of plectin in tissues. J Cell Biol 97, 887–901.
Windoffer R, Schwarz N, Yoon S, Piskova T, Scholkemper M, Stegmaier J, Bonsch A, Di Russo J, Leube RE (2022). Quantitative mapping of keratin networks in 3D. Elife 11, e75894.
Yang S, Zhao C, Ren J, Zheng K, Shao Z, Ling S (2022). Acquiring structural and mechanical information of a fibrous network through deep learning. Nanoscale 14, 5044–5053.
Yu W, Khandelwal P, Apodaca G (2009). Distinct apical and basolateral membrane requirements for stretch-induced membrane traffic at the apical surface of bladder umbrella cells. Mol Biol Cell 20, 282–295.
Yu Z, Liao J, Chen Y, Zou C, Zhang H, Cheng J, Liu D, Li T, Zhang Q, Li J, *et al*. (2019). Single-cell transcriptomic map of the human and mouse bladders. J Am Soc Nephrol 30, 2159–2176.